# Deep learning tools and modeling to estimate the temporal expression of cell cycle proteins from 2D still images

Thierry Pécot[1], Maria C. Cuitiño[2], Roger H. Johnson[3], Cynthia Timmers[4*], and Gustavo Leone[3]

[1]Department of Biochemistry and Molecular Biology, Hollings Cancer Center, Medical University of South Carolina, Charleston, SC 29425, USA

[2]Department of Radiation Oncology, Arthur G. James Hospital/Ohio State Comprehensive Cancer Center, Columbus, OH 43210, USA

[3]Cancer Center, Medical College of Wisconsin, Milwaukee, WI 53226, USA

[4]Division of Hematology and Oncology, College of Medicine, Medical University of South Carolina, Charleston, SC 29425, USA

*Currently at Incyte Corporation

## ABSTRACT

Automatic characterization of fluorescent labeling in intact mammalian tissues remains a challenge due to the lack of quantifying techniques capable of segregating densely packed nuclei and intricate tissue patterns. Here, we describe a powerful deep learning-based approach that couples remarkably precise nuclear segmentation with quantitation of fluorescent labeling intensity within segmented nuclei, and then apply it to the analysis of cell cycle dependent protein concentration in mouse tissues using 2D fluorescent still images. First, several existing deep learning-based methods were evaluated to accurately segment nuclei using different imaging modalities with a small training dataset. Next, we developed a deep learning-based approach to identify and measure fluorescent labels within segmented nuclei, and created an ImageJ plugin to allow for efficient manual correction of nuclear segmentation and label identification. Lastly, using fluorescence intensity as a readout for protein concentration, a three-step global estimation method was applied to the characterization of the cell cycle dependent expression of E2F proteins in the developing mouse intestine. Additional spatial analysis of the data revealed a correlation between cell cycle progression and location of nuclei within the intestinal epithelium.

## INTRODUCTION

Automatic image analysis is at the core of human and animal tissue-based research. However, quantitation of morphological features or fluorescent labeling in intact mammalian tissues still remains a challenge. The densely packed nuclear aggregates that characterize many of these tissues,

the extensive variability across different tissue types, and the continuously increasing number of imaging modalities are some of the many variables that make tissue biological quantification an extremely difficult task. Over the last decade (Cireşan et al. 2012, Krizhevsky et al. 2012, LeCun et al. 2015, Schmidhuber 2015), deep learning has brought artificial intelligence to the forefront of image-based decision making. In particular, deep convolutional neural networks have demonstrated their superiority for image segmentation (Cireşan et al. 2012, Hollandi et al. 2020, Krizhevsky et al. 2012, Moen et al. 2019). However, this machine learning-based approach requires large amounts of annotated data and new strategies have to be developed to process highly complex biological objects acquired with different modalities by considering small training datasets. In this paper, we propose a series of deep learning-based approaches to precisely segment nuclei and to identify fluorescently labelled cells in order to analyze the evolution of cell cycle dependent E2F protein concentration in mouse tissues.

E2Fs are major regulators of the cell cycle. The members of this family of transcription factors are categorized into three subclasses in mammals: canonical activators (E2F1-3A/B), canonical repressors (E2F4-6), and atypical repressors (E2F7-8) (Chen et al. 2009, Iaquinta & Lees 2007, Lammens et al. 2009, Logan et al. 2005). Adding to the body of literature on E2F-dependent transcriptional activity in vivo, our lab previously provided quantitative evidence on the temporal expression of representative activator (E2F3A), canonical repressor (E2F4) and atypical repressor (E2F8) family members during embryonic development (Cuitiño et al. 2019), all of which have been shown to be of major importance (Humbert et al. 2000, Li et al. 2008, Rempel et al. 2000, Tsai et al. 2008). To establish the temporal expression profiles of the three sentinel E2Fs, we used

an E2F3A specific antibody and generated MYC-tagged E2F4/E2F8 knock-in mice. In addition to fluorescence labeling of E2F3A, E2F4 and E2F8, 5-ethynyl-2'-deoxyuridine (EdU) and Histone H3 S10 phosphorylation (pH3) were used to identify S, G2 and M phases. Images of eight different combinations of markers were acquired from sections of the developing mouse intestine using confocal and widefield microscopy (see Fig. 1). The data analysis pipeline consisted of i) nuclear segmentation with a deep learning approach (Van Valen et al. 2016), ii) nuclear marker identification by thresholding, and iii) estimation of E2F concentrations over the cell cycle from 2D intensity histograms.

In this manuscript, we propose and evaluate alternative methods to quantify nuclear protein levels which result in an improved automated pipeline with greatly reduced requirement for interactive manual corrections. Using a small training dataset composed of 2D still images (with and without various forms of data augmentation), we first evaluate three different deep learning strategies to segment nuclei in microscopic images of embryonic mouse intestinal epithelium. We also design post-processing methods to improve nuclear segmentation. We then propose another deep learning-based approach for identifying nuclear markers in the epithelial cells and demonstrate the superiority of this method to the usual threshold based method (Blom et al. 2017, Keren et al. 2018). Finally, we create an ImageJ plugin (Schindelin et al. 2012, Schneider et al. 2012) named *Annotater* to specifically and efficiently correct nuclear segmentation and marker identification, ensuring that nuclear features are accurately quantified.

From the image features extracted from 2D still images, we perform temporal analysis to

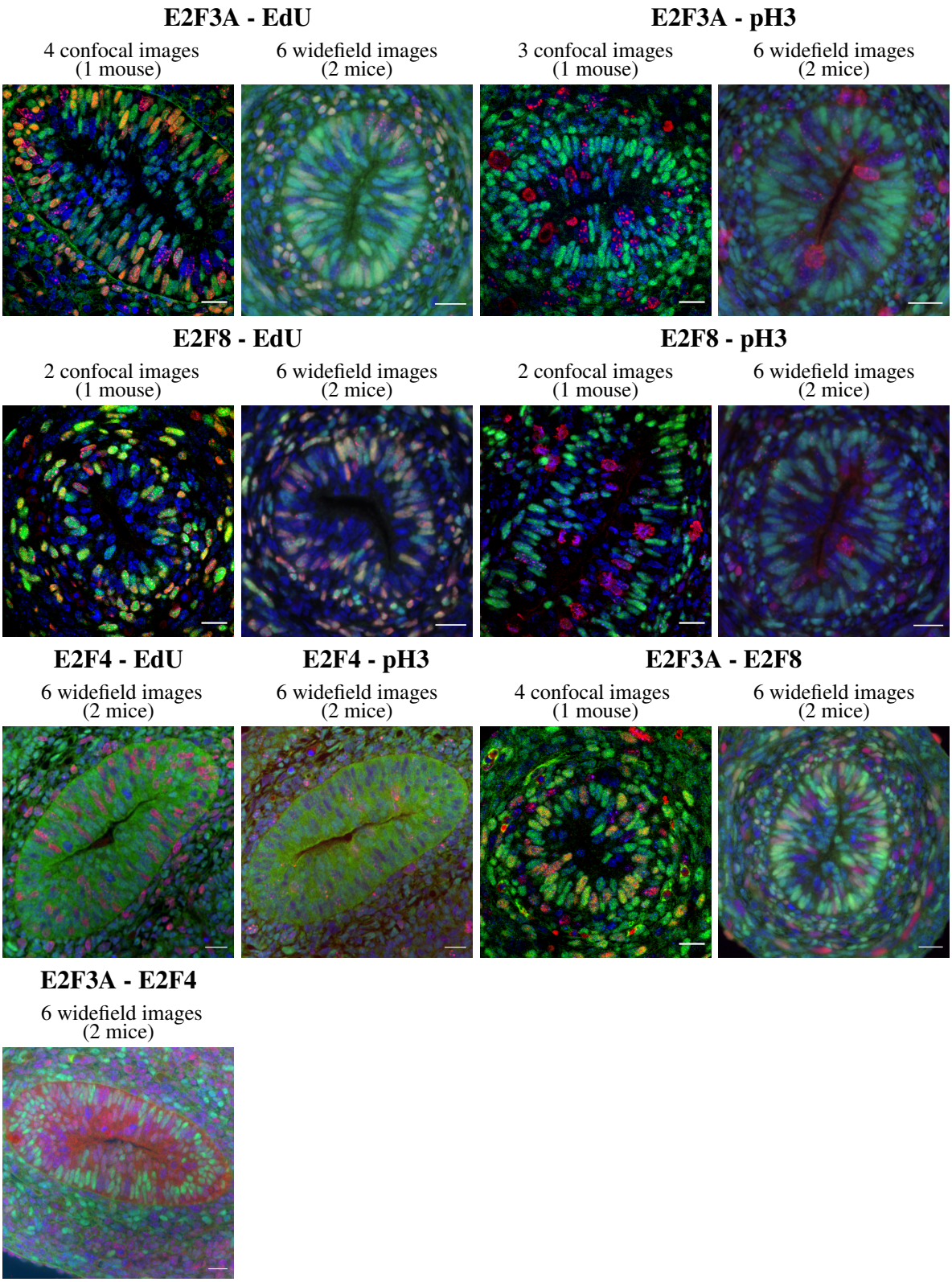


Figure 1: **Example images.** One example for each combination of markers and modality for fluorescence images used in the study. The combination of markers, number of images of each type, modality, and number of mice used in the study are shown on top of the images. Note the small size of the training set. Scale bar = 20µm.

E2F protein concentration over the cell cycle and spatiotemporally characterize the movement of intestinal epithelial cell nuclei in relation to cell cycle phases. Based on three mathematical assumptions grounded in cell biology, we initialize the temporal evolution of E2F concentrations using a graph optimization method. Cell cycle markers are then used to temporally register E2F proteins' concentration with respect to cell cycle phase. Finally, the global estimation of the protein concentration of E2F3A, E2F4 and E2F8 through the cell cycle is defined as an assignment problem and solved with the Hungarian algorithm (Kuhn 1955, Munkres 1957). By combining the temporal expression of selected E2Fs and the apico-basal location of E2F-expressing nuclei in the developing mouse intestine, we provide supporting evidence to the notion that nuclear positioning changes in association with the cell cycle.

## RESULTS

### Mask R-CNN is the optimal deep learning approach for segmenting nuclei in cross-sectional images of complex tissues

Over the last decade, deep learning has revolutionized computer vision (Cireşan et al. 2012, Krizhevsky et al. 2012, LeCun et al. 2015, Schmidhuber 2015). Over the years, several deep learning approaches have been successfully applied to segment cell nuclei (Cireşan et al. 2013, Ronneberger et al. 2015, Van Valen et al. 2016). More recently, the 2018 data science bowl (Caicedo et al. 2019) attempted to definitely solve this problem in 2D by posing the challenge: Create an algorithm for automated nuclei detection. Although impressive results were obtained for different

light microscopy modalities and a variety of nuclear stains (Hollandi et al. 2020), nuclear segmentation from complex tissues such as intestinal epithelium still represents an unusually challenging problem. As is the case for most biological imaging studies due to natural variability in the objects of interest that are captured using dissimilar imaging modalities, no annotated data is available for this specific application. Consequently, we set out with the goal of designing a robust approach that would lend itself to routine use in the typical biology laboratory. We evaluated three different deep learning approaches for nuclear segmentation: U-Net (Falk et al. 2019, Ronneberger et al. 2015), Inception-V3 (Szegedy et al. 2016) and Mask R-CNN (He et al. 2017). U-Net, perhaps the most-used deep convolutional neural network for biomedical data, is composed of an encoder part, used to capture image features, and a decoder part to estimate a class at each pixel of the input images (Fig. 2 - Fig. supp. 1 **a**). Inception-V3, which was designed to identify objects in images, is a deep convolutional neural network that only estimates one class given an input image (Fig. 2 - Fig. supp. 2 **a**). When using this architecture for nuclear segmentation, inputs are defined as image patches and the output corresponds to the class at the patch center. Inception-V3 is much slower than U-Net for both training and processing (Fig. 2 - Fig. supp. 2 **d**), as a decision is only made for the central pixel of the input image patch, in contrast to a decision being made at each pixel of the input image as it is in U-Net. For both U-Net and Inception-V3, three classes are defined: inner nuclei, nuclei contours, and background (Caicedo et al. 2019, Van Valen et al. 2016). Individual nuclei are then obtained by subtracting the nuclei contours from the inner nuclei (see Methods). To improve performance, we developed a post-processing method that we call corrected watershed, wherein the results obtained with the U-Net or Inception-V3 network are combined with those

produced by the watershed method (Vincent & Soille 1991) (see Methods). Mask R-CNN first extracts image features using a backbone convolutional neural network (Fig. 2 - Fig. supp. 3 **a**). From these features, a Region Proposal Network (RPN) submits subregions of the input image, a fully connected neural network defines a class and a bounding box for the input subregions, and a convolutional neural network generates a segmentation mask for the same input subregions. In our study, the only class corresponds to nuclei. When processing, a score is obtained for each subregion proposed by the RPN to make a decision about the existence of a nucleus. With this approach, the output corresponds directly to individual nuclei.

As proposed by Caicedo *et al.* (2019), we use the F1 score with respect to the Intersection over Union (IoU) to compare performance of the three deep learning approaches (see Methods). There are two aspects to performance: 1) the ability to correctly identify all nuclei in an image, which is the same as detecting the correct number of nuclei, and 2) the accuracy of the nuclear contours created in the output. This second aspect of performance is quantified by the F1 score over a range of IoU values. The IoU of two objects is the ratio of the intersection to the union of their areas. With an IoU of at least 0.5 (within the range 0.5-1.0), only two nuclei, one from the ground truth as determined by a pathologist and one estimated with a given method, can be paired. The F1 score for an IoU equal to 0.5 can be used to assess the ability of a method to accurately identify all nuclei. F1 scores for IoU thresholds in the range 0.5-1.0 reflect the localization precision of the segmentation, which means the accuracy of the defined nuclear contours.

Fig. 2 shows the superiority of the Mask R-CNN method for both modalities. The results

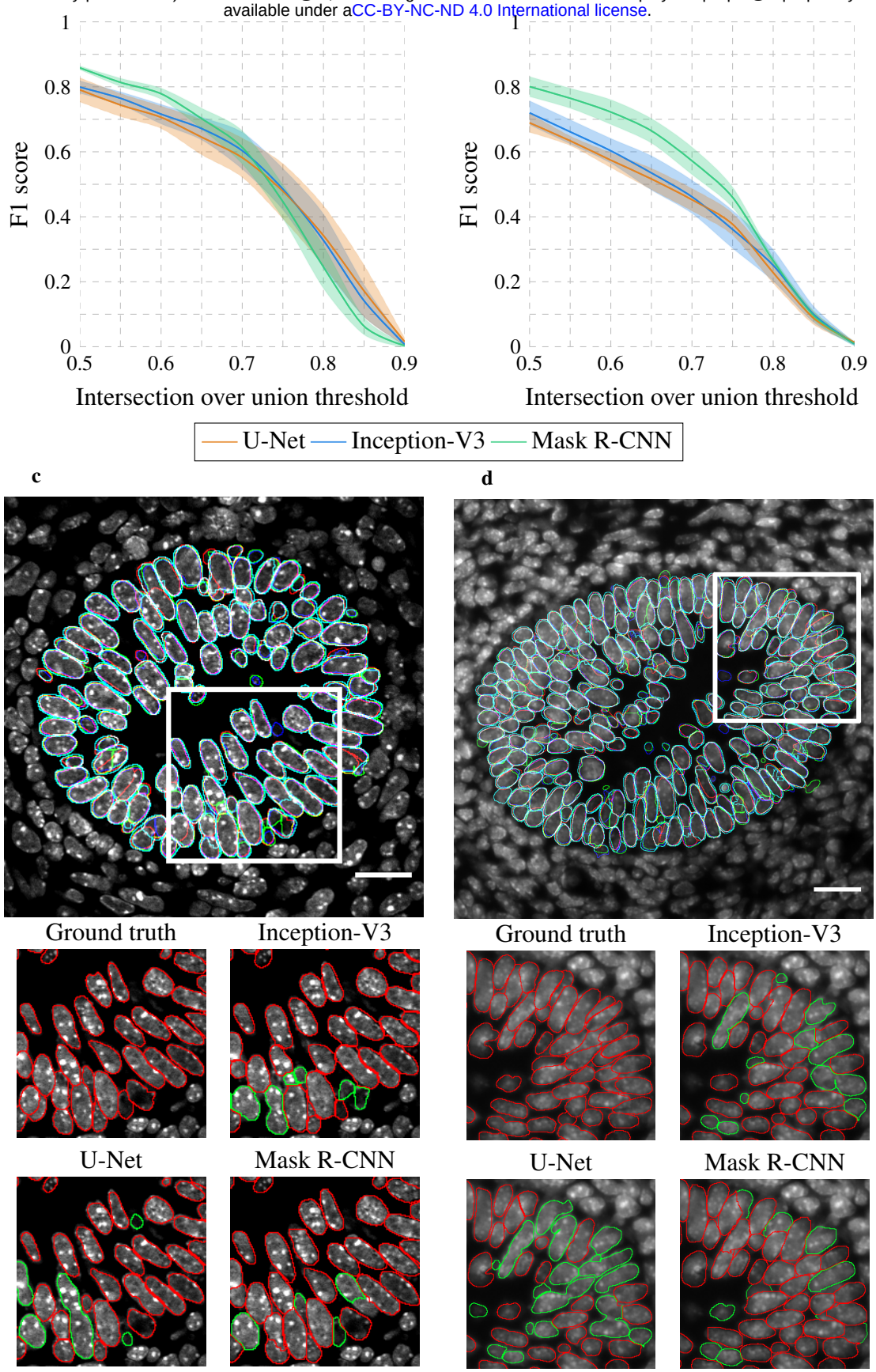


Figure 2: **Comparison of U-Net, Inception-V3 and Mask R-CNN for nuclear segmentation. a-b** F1 score for range of IoU thresholds obtained with the U-Net, Inception-V3 and Mask R-CNN approaches for confocal **a** and widefield **b** images. Lines correspond to average F1 score over the three tested images while the shaded areas represent the standard error. **c-d** Segmented nuclei obtained with the U-Net (blue), Inception-V3 (green) and Mask R-CNN (cyan) as well as the ground truth (red) for confocal **c** and widefield **d** images. White inset rectangles in top images are shown at higher magnification below for the ground truth and each approach. In high-mag images, correctly identified nuclei are outlined in red, incorrectly in green. Scale bar = 20µm.

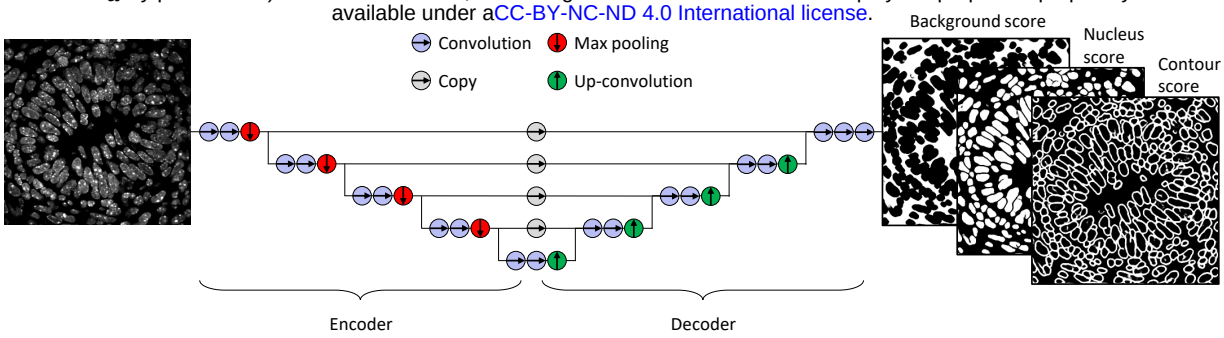


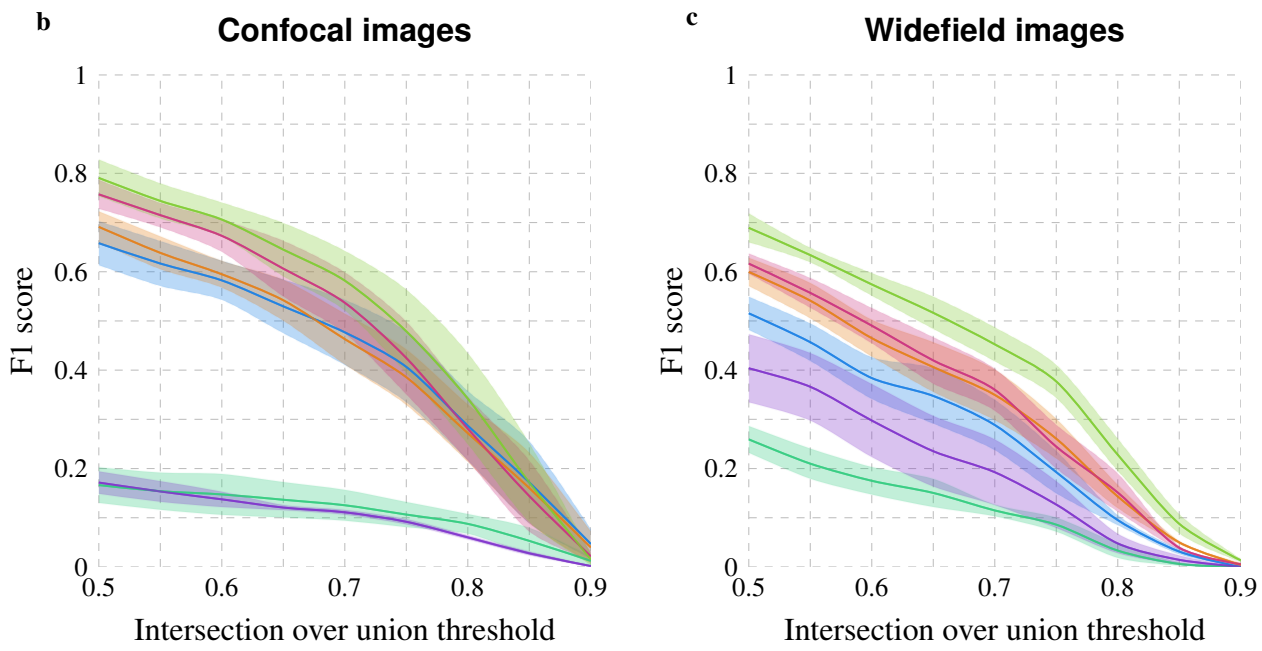


**d**

| | **Computation time** on a Nvidia Titan XP GPU |
|---|---|
| **Training** (9 training + 3 validation confocal images) | 1 min 9 s |
| **Training** (37 training + 8 validation widefield images) | 3 min 22 s |
| **Training** (46 training + 11 validation confocal and widefield images) | 4 min 6 s |
| **Training** with data augmentation (9 training + 3 validation confocal images) | 4 h |
| **Training** with data augmentation (37 training + 8 validation widefield images) | 15 h |
| **Training** with data augmentation (46 training + 11 validation confocal and widefield images) | 20 h |
| **Running** (512x512 image) | 21 s |
| **Running + corrected watershed** (512x512 image) | 24 s |

Figure 2 supplement 1: **Evaluation of U-Net for nuclear segmentation.** **a** U-Net architecture with example input image and outputs. **b-c** F1 score over a range of IoU thresholds obtained with the U-Net approach by training on confocal or widefield images, by training on confocal and widefield images, by training on confocal or widefield images with watershed postprocessing, without or with data augmentation, applied to confocal **b** and widefield **c** images. Lines correspond to average F1 score while shaded areas represent standard error. **d** Computation time to train a U-Net classifier on confocal, widefield or both confocal and widefield images, without and with data augmentation, as well as computation time to process a 512 x 512 image without and with corrected watershed postprocessing.

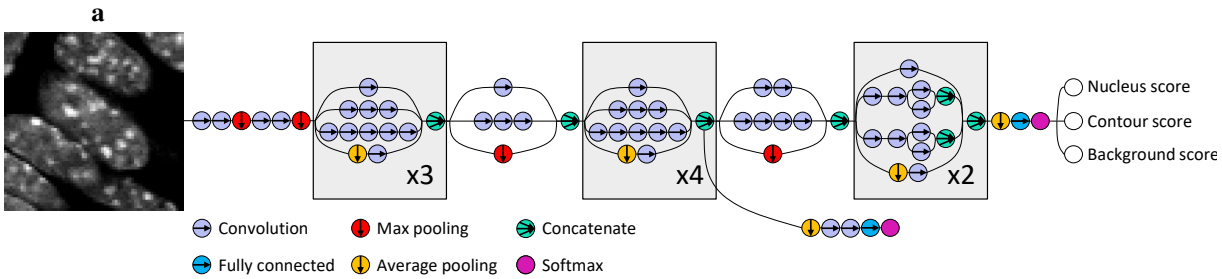


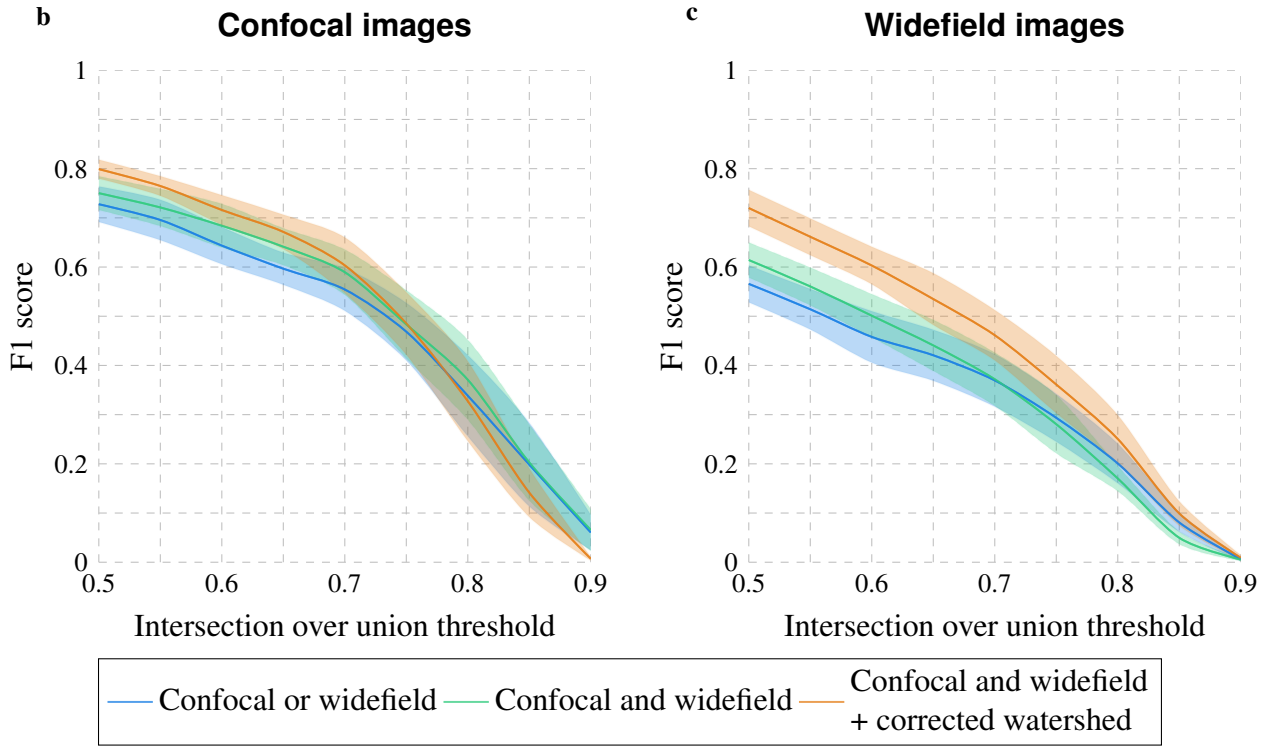


**d**

| | **Computation time** on a Nvidia Titan XP GPU |
|---|---|
| **Training** (12 training confocal images) | 30 h |
| **Training** (45 training widefield images) | 94 h |
| **Training** (57 training confocal and widefield images) | 115 h |
| **Running** (512x512 image) | 3 min 50 s |
| **Running + corrected watershed** (512x512 image) | 3 min 53 s |

Figure 2 supplement 2: **Evaluation of Inception-V3 for nuclear segmentation. a** Inception-V3 architecture. **b-c** F1 score over a range of IoU thresholds obtained with the Inception-V3 approach by training on confocal or widefield images without and with corrected watershed postprocessing, and by training on confocal and widefield images with corrected watershed postprocessing for confocal **b** and widefield **c** images. Lines correspond to average F1 score while shaded areas represent the standard error. **d** Computation time to train an Inception-V3 classifier on confocal, widefield or both confocal and widefield images as well as computation time to process a 512 x 512 image without and with corrected watershed postprocessing.

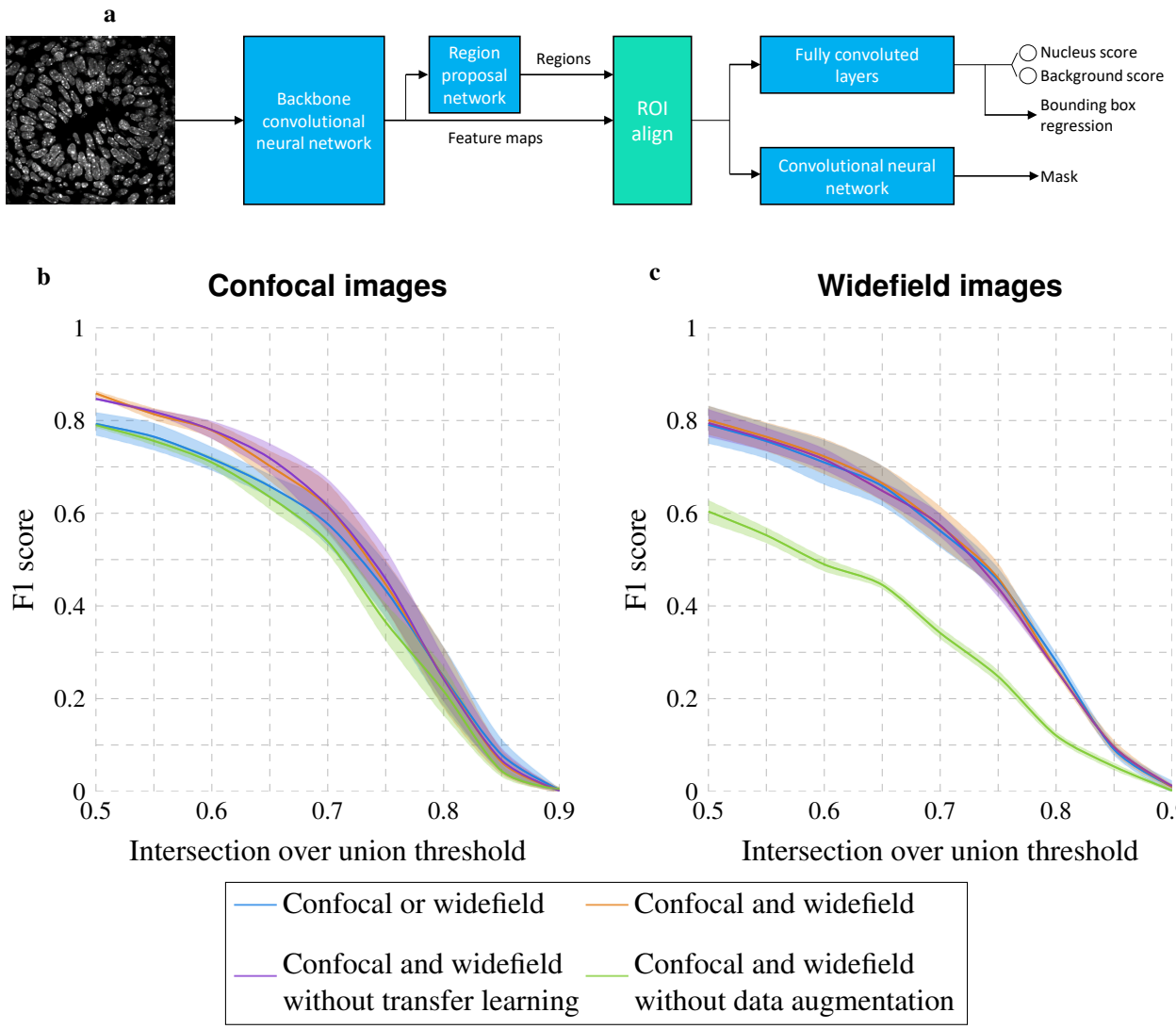


**d**

| | **Computation time** on a Nvidia Titan XP GPU |
|---|---|
| **Training** (9 training + 3 validation confocal images) | 1h |
| **Training** (37 training + 8 validation widefield images) | 3 h 55 min |
| **Training** (46 training + 11 validation confocal and widefield images) | 4 h 50 min |
| **Training** with data augmentation (9 training + 3 validation confocal images) | 3 h 10 min |
| **Training** with data augmentation (37 training + 8 validation widefield images) | 7 h 30 min |
| **Training** with data augmentation (46 training + 11 validation confocal and widefield images) | 9 h 20 min |
| **Running** (512x512 image) | 28 s |

Figure 2 supplement 3: **Evaluation of Mask R-CNN for nuclear segmentation. a** Mask R-CNN architecture. **b-c** F1 score over a range of IoU thresholds obtained with the Mask R-CNN approach by training on confocal or widefield images, by training on confocal and widefield images with both transfer learning and data augmentation, by training on confocal and widefield images without transfer learning, and by training on confocal and widefield images without data augmentation for confocal **b** and widefield **c** images. Lines correspond to average F1 score while shaded areas represent the standard error. **d** Computation time to train a Mask R-CNN classifier on confocal, widefield or both confocal and widefield images, with and without data augmentation, as well as the computation time to process a 512 x 512 image.

represent the best performance of each deep learning method from among the algorithmic variants that invoke combinations of transfer learning, data augmentation and watershed correction as discussed below in connection with Figs. 1, 2 and 3.

As shown in Fig. 2 **a-b**, and emphasized in the magnified images of Fig. 2 **c-d**, the U-Net method produced the worst results. Data augmentation, a process that artificially and massively increases the size of the training dataset by applying mathematical operations such as adding noise and rotating or flipping the images (see Methods), improves the segmentation accuracy (Fig. 1 **b-c**). However, pooling together confocal and widefield images in the training dataset produces considerably worse segmentation accuracy compared to training on only confocal or only on widefield images. This demonstrates the inability of the U-Net approach to generalize nuclear segmentation with a small training dataset.

In contrast, the Inception-V3 approach obtains better results when both modalities are used in the training dataset (Fig. 2 - Fig. supplement 2 **b-c**). While for Inception-V3 the training dataset was not increased via data augmentation because the computation time is already long, the high degree of overlap between input patches to which mathematical operations are applied (see Methods) produces an effect similar to data augmentation, explaining in part the improved performance of the Inception-V3 approach relative to U-Net. Because Inception-V3 estimates the class one pixel at a time, both training and processing are highly compute intensive and not feasible in practice (Fig. 2 - Fig. supplement 2 **d**). The proposed corrected watershed post-processing improves the results obtained for both U-Net and Inception-V3 (Figs. 1-2 **b-c**).

The Mask R-CNN method obtains the best nuclear segmentation for both modalities (Fig. 2), in large part due to the improvement realized through data augmentation and also to the transfer learning from the coco dataset (Lin et al. 2014), (Fig. 2 - Fig. supplement 3 **b-c**). Combining confocal and widefield images in the training dataset improves the results, especially for confocal images (Fig. 2 - Fig. supplement 3 **b-c**). This demonstrates how Mask R-CNN can benefit from an increase in training dataset size (from 9 training and 3 validation images for confocal alone to 46 training and 11 validation images when pooled with widefield) even if the data are not uniform, coming from different sources. Moreover, training and processing are fast (Fig. 2 - Fig. supplement 3 **d**), and the results do not require any post-processing. One limitation of the Mask R-CNN method compared with U-Net and Inception-V3 is an inferior boundary localization accuracy for confocal images, as demonstrated by the lower F1 scores for IoU threshold values greater than 0.75 (Fig. 2 **a**). Due to slightly larger nuclear masks (cyan boundaries in Fig. 2 **c**), this limitation is more than compensated for by Mask R-CNN's higher true positive nuclei identification rate in most biological applications. While the performance of Mask R-CNN is impressive, its accuracy is not perfect and may be insufficient for many applications. Therefore, we designed the ImageJ plugin Annotater (see Methods), a tool that allows users to efficiently correct the nuclear segmentation.

**Deep learning improves identification of fluorescent nuclear markers**

Identifying nuclear markers amounts to querying the fluorescent signal inside the identified nuclei. Typically, a thresholding procedure is applied (Blom et al. 2017, Keren et al. 2018), but this approach is not always accurate, especially when different patterns of fluorescence over a wide range

of intensities are involved as is the case for EdU and pH3 (see diffuse and punctate patterns in Fig. 3). To improve accuracy, we tested a deep learning approach for nuclear marker identification. As the goal is not to identify regions but to make a decision for each nucleus regarding the presence/absence of an E2F or the diffuse/punctate/absence of EdU or pH3, the Mask R-CNN and U-Net approaches are not suitable. In contrast, with an input defined as an image patch centered on each nucleus, the Inception-V3 architecture is appropriate to decide about the presence, potentially in diffuse or punctate state, or absence of a marker. In addition to data augmentation, we also define a so-called pixel-based training dataset (as opposed to nuclei-based training dataset) that includes the input patches centered at each pixel belonging to the nuclei (see Methods). This strategy has a similar effect to data augmentation, as it drastically increases the training dataset. Although DAPI staining is different from the nuclear markers used to identify the E2Fs, EdU and pH3, the images are acquired simultaneously, so the image features captured by the Inception-V3 method for nuclear segmentation are potentially meaningful to identify nuclear markers. Consequently, we also perform transfer learning from the nuclear segmentation (see Methods). To easily set the threshold for marker identification, we designed an interface in the Annotater that we used to obtain the results shown in Fig. 3 for manual thresholding.

As shown in Fig. 3, compared to manual thresholding, the Inception-V3 approach provides better performance for each marker in both modalities. Manual thresholding achieves a relatively good performance for E2F3A and E2F8 identification in both modalities, and for pH3 in confocal images. The latter might appear surprising, but the two different patterns for pH3 in confocal images are different enough to allow a strategy based on the thresholded area in the nuclei (see

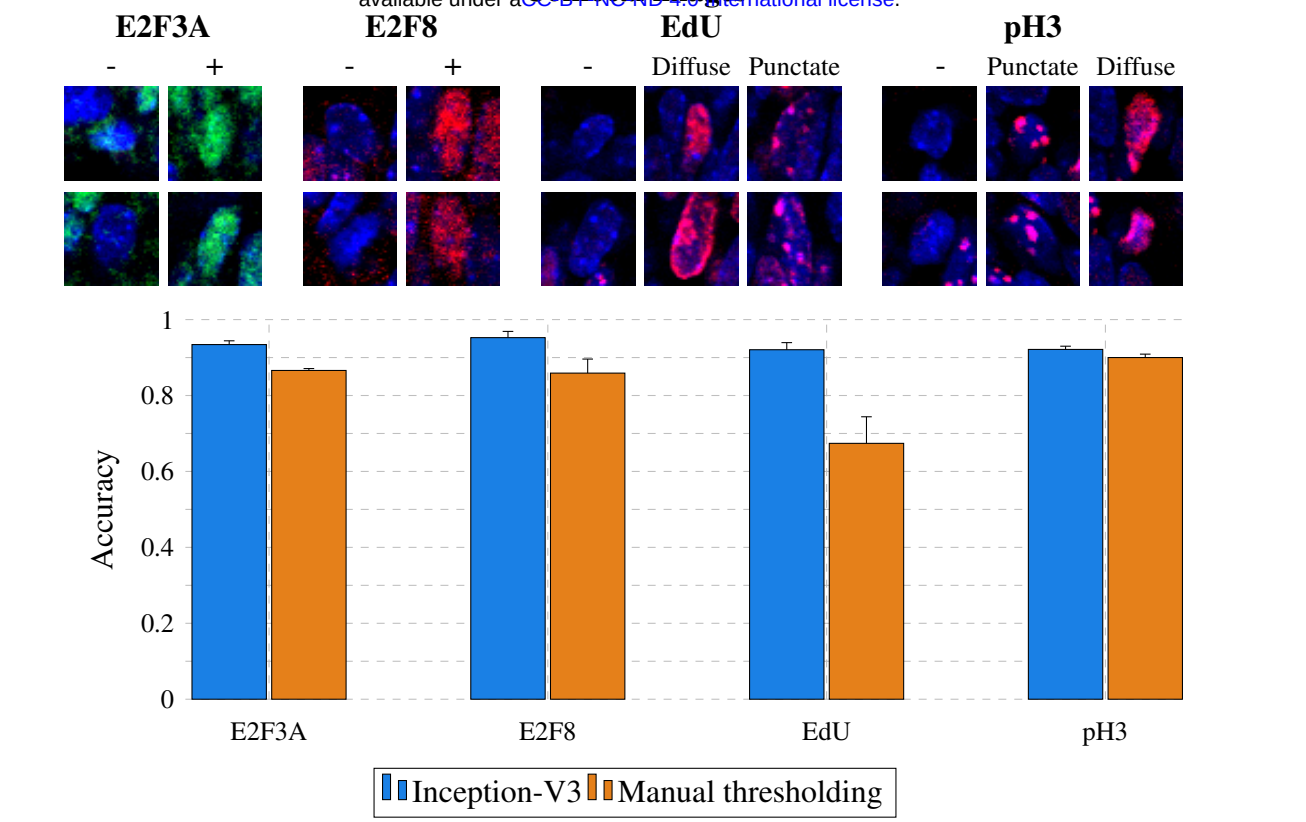


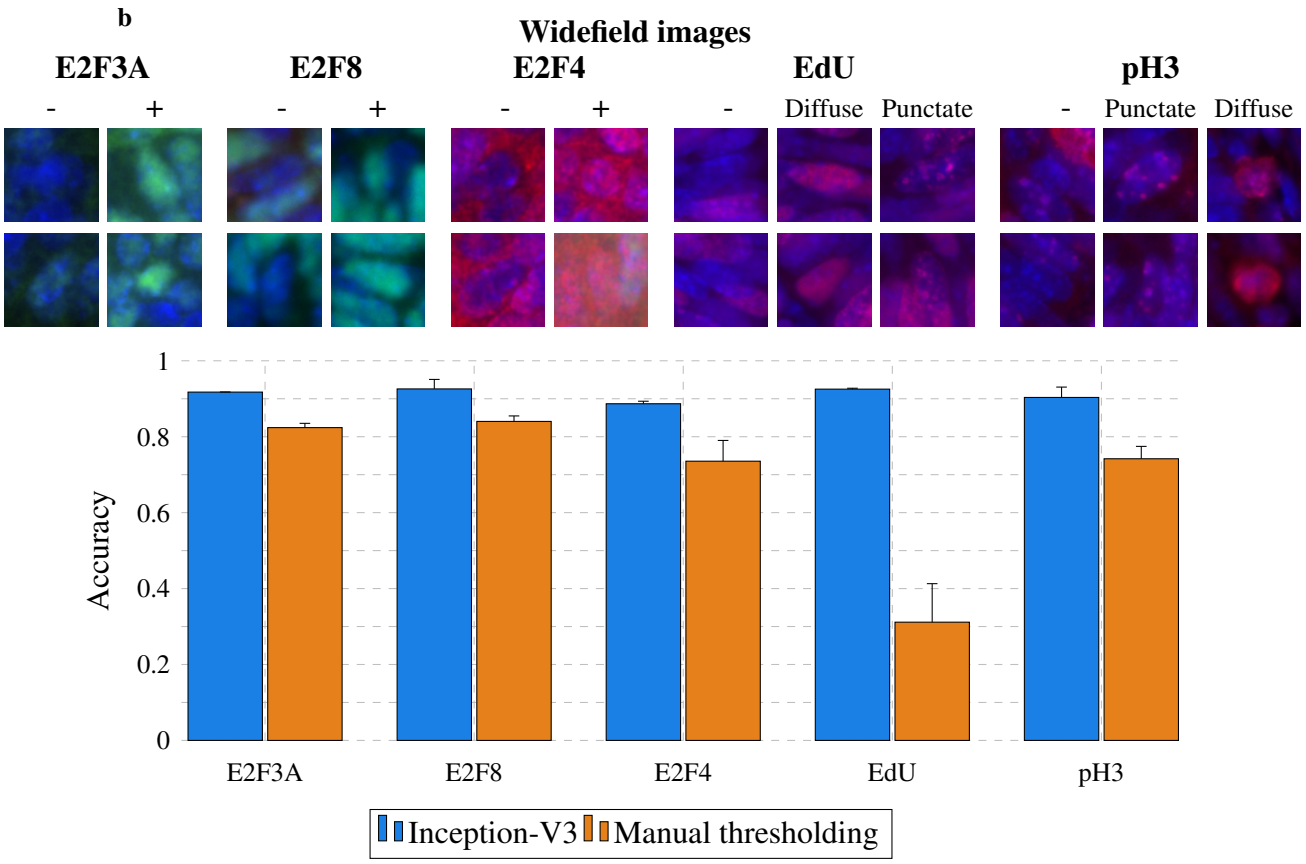


Figure 3: **Comparison between Inception-V3 and manual thresholding for marker identification. a-b** Top rows (images): examples of E2F3A-, E2F8- and E2F4-positive and -negative nuclei, as well as EdU- and pH3-negative, diffuse and punctate nuclei in **a** confocal and **b** widefield images. Bottom rows (bar graphs): Accuracy obtained with the Inception-V3 and manual thresholding approaches for marker identification of E2F3A, E2F8, E2F4, EdU and pH3 in **a** confocal and **b** widefield images. Bars denote average accuracy; error bars represent the standard error.

**a**

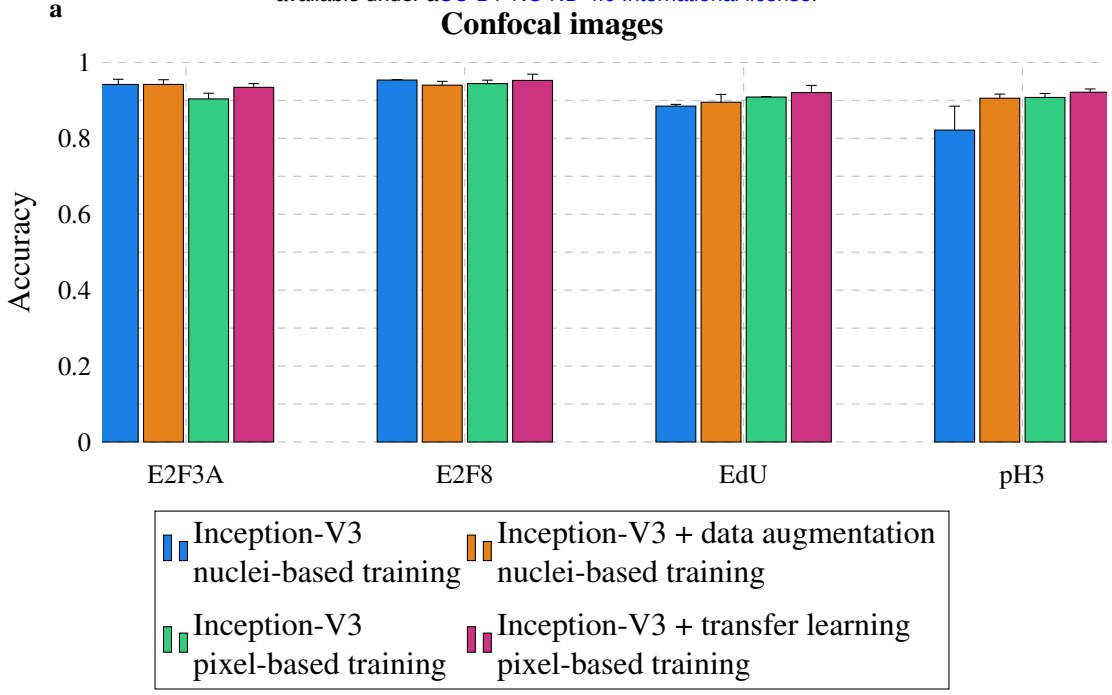


**b**

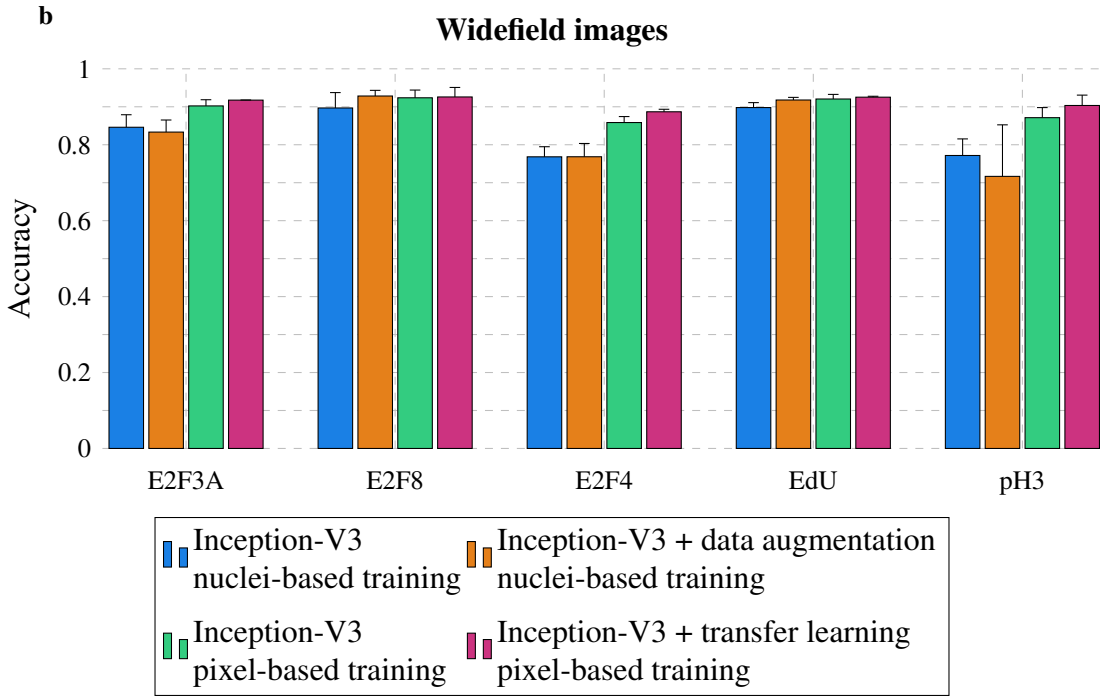


**c**

| | **Computation time** on a Nvidia Titan XP GPU |
|---|---|
| **Nuclei-based training** (12 images) | 1 h 7 min |
| **Nuclei-based training with data augmentation** (12 images) | 4 h |
| **Pixel-based training** (12 images) | 11 h 50 min |
| **Pixel-based training with transfer learning** (12 images) | 13 h |
| **Running** (512x512 image) | 5 s |

Figure 3 supplement 1: **Performance of Inception-V3 for marker identification. a-b** Inception-V3 accuracy with and without transfer learning for marker identification of E2F3A, E2F8, E2F4, EdU and pH3 in **a** confocal and **b** widefield images. Bars correspond to average accuracy; error bars to standard error. **c** Computation time to train on 12 images with and without transfer learning, and computation time to process a 512 x 512 image.

Methods) to lead to satisfying results (Fig. 3 **a**). However, the results for E2F4, Fig. 3 **b**, are not as good: Because E2F4 is also cytoplasmic, the extra-nuclear fluorescence confounds the thresholding decision. Finally, thresholding clearly fails to identify the two different patterns (diffuse, punctate) of EdU in images from both modalities as well as the patterns of pH3 in widefield images. In contrast, the Inception-V3 approach yields accuracies greater than 90% for all markers except E2F4 (89%) (Fig. 3). As shown in Fig. 3 supp. 1 **a-b**, the use of the pixel-based training datasets does not significantly improve marker identification for confocal images, but does improve performance on E2F3A, E2F4 and pH3 markers in widefield images. Additionally, the transfer learning from the nuclear segmentation slightly improves the results for all markers in both modalities. Computation (after training) is fast because only one decision is made per nucleus (Fig. 3 supp. 1 **c**). Overall, this study demonstrates the remarkable accuracy of the deep learning-based approach in identifying cells that are positive for the tested nuclear markers, not only when the marker is both nuclear and cytoplasmic, but also when it exhibits different labeling patterns, such as diffuse and punctate. Given such a high level of accuracy, correcting the results with the Annotater plugin takes only a short time.

**Estimation of E2F accumulation over the cell cycle from 2D still images**

The most straightforward way to assess the evolution of a protein's concentration over the cell cycle would be to monitor the expression level in every cell through all phases of the cycle. However, this is not possible in the proliferative tissue of a living animal. Instead of observing one cell, we propose to observe a large population of cells, each corresponding to a snapshot characterizing the

cell state at a particular time during the cell cycle, and to reconstruct protein concentration as a function of time in the cell cycle by combining all these snapshots. We assume that fluorescence intensity is proportional to protein concentration (Lo et al. 2015) and therefore define four levels of intensity for E2Fs (see Methods). The negative cells have an intensity equal to 0. In each individual image, we measure the average fluorescence intensity for each positive cell. Within each image, the range of intensity from the lowest average intensity to the highest is divided into three bins that define levels 1, 2 and 3. On the other hand, EdU and pH3 markers are defined by their diffuse and punctate states, which change as a function of cell cycle phase. As shown in our previous work (Cuitiño et al. 2019), EdU shows a diffuse pattern during the first half of S phase and a punctate pattern during the second half of S phase. pH3 shows a punctate pattern during the second half of S phase and G2 and a diffuse pattern during mitosis. These two markers allow us to register E2Fs expression with respect to the cell cycle. We propose to globally estimate the E2F concentration's evolution over the cell cycle in three steps: i) initialization, ii) cell cycle registration and iii) global optimization. In this paper, as in our previous manuscript (Cuitiño et al. 2019), the phrase "protein accumulation" is synonymous with "protein concentration" and connotes this balance between production and degradation, regardless of whether the protein concentration is increasing or decreasing. Also in this paper, the fluctuation over time of a quantity such as fluorescence intensity or protein accumulation is referred to as "evolution," which is therefore synonymous with "time course."

We use the term "initialize" to mean creation of a first estimate of protein accumulation over the cell cycle: a graph of fluorescence intensity vs. time. To initialize all combinations of markers

from the images (see Fig. 1), we make three fundamental assumptions:

1 The number of cells in a given phase of the cell cycle is proportional to the duration of that phase.

2 Temporal evolution of protein accumulation is similar in all observed cells.

3 Concentrations of E2Fs are concave downward parabolas, *i.e.* they increase from 0 to their maximum and then decrease from this maximum to 0.

These assumptions are validated by the following biological statements:

1 Proliferation in intestinal epithelium is asynchronous, so each cell cycle phase is observed at a frequency proportional to its duration.

2 All cells in intestinal epithelium are proliferating and undergo cell cycle at a uniform rate.

3 Cell cycle-regulated proteins first accumulate over time and are then degraded.

We use 2D histograms to initialize protein accumulation (Figs. 4 supp. 1-2). In these histograms, the first axis corresponds to the intensity of an E2F, while the second axis corresponds to either another E2F intensity or the states of EdU or pH3 staining. From these histograms, we define graphs with costs associated with edges reflecting the possible intensity/pattern transitions of the E2Fs, EdU and pH3. The sequence of edges that goes through all vertices with minimum cost is used to initialize the evolution of protein accumulation over time (Figs. 4 supp. 1-2 and Methods).

The initializations obtained for all eight different combinations of markers are shown in Fig. 4 supp. 3. As EdU and pH3 labeling patterns with respect to the cell cycle are known, we then register E2Fs with respect to EdU and pH3 through a circular permutation (see Methods). We use the same approach to refine EdU labeling during the cell cycle (see Methods). The protein accumulations after registration are shown in Fig. 4 supp. 4. We finally model the global estimation of E2F accumulation over the cell cycle as an assignment problem. We use the Hungarian algorithm (Kuhn 1955, Munkres 1957) to successively estimate the individual accumulation of each E2F over the cell cycle given the EdU and pH3 patterns as constraints (see Methods). We also add a local constraint to only allow growing substitutions for E2Fs (see Methods). The final result is shown in Fig. 4, depicting the successive waves of E2F3A, E2F4 and E2F8 over the cell cycle.

**Movement of epithelial cell nuclei between basal and apical surfaces in relation to cell cycle**

Nuclear spatial positioning within pseudostratified epithelia during embryonic development has been shown to be associated with cell cycle (Grosse et al. 2011). Consistent with the notion that mitosis occurs apically in the embryonic intestinal epithelium, we observed that most pH3 diffuse nuclei in our study were located in the vicinity of the lumen (Fig. 5 supp. 1, blue contours). To quantitatively test this observation, we looked at the distribution of pH3 punctate and pH3 diffuse nuclei across experiments using QuantEv (Pécot et al. 2018). As shown in Fig. 5 **a**, the majority of pH3 diffuse nuclei were located near the lumen. It should be noted that 2D images are used, and therefore delineation of the lumen might not be entirely accurate owing to plane of section effects. Several studies have also shown that DNA synthesis occurs in nuclei that are located basally within

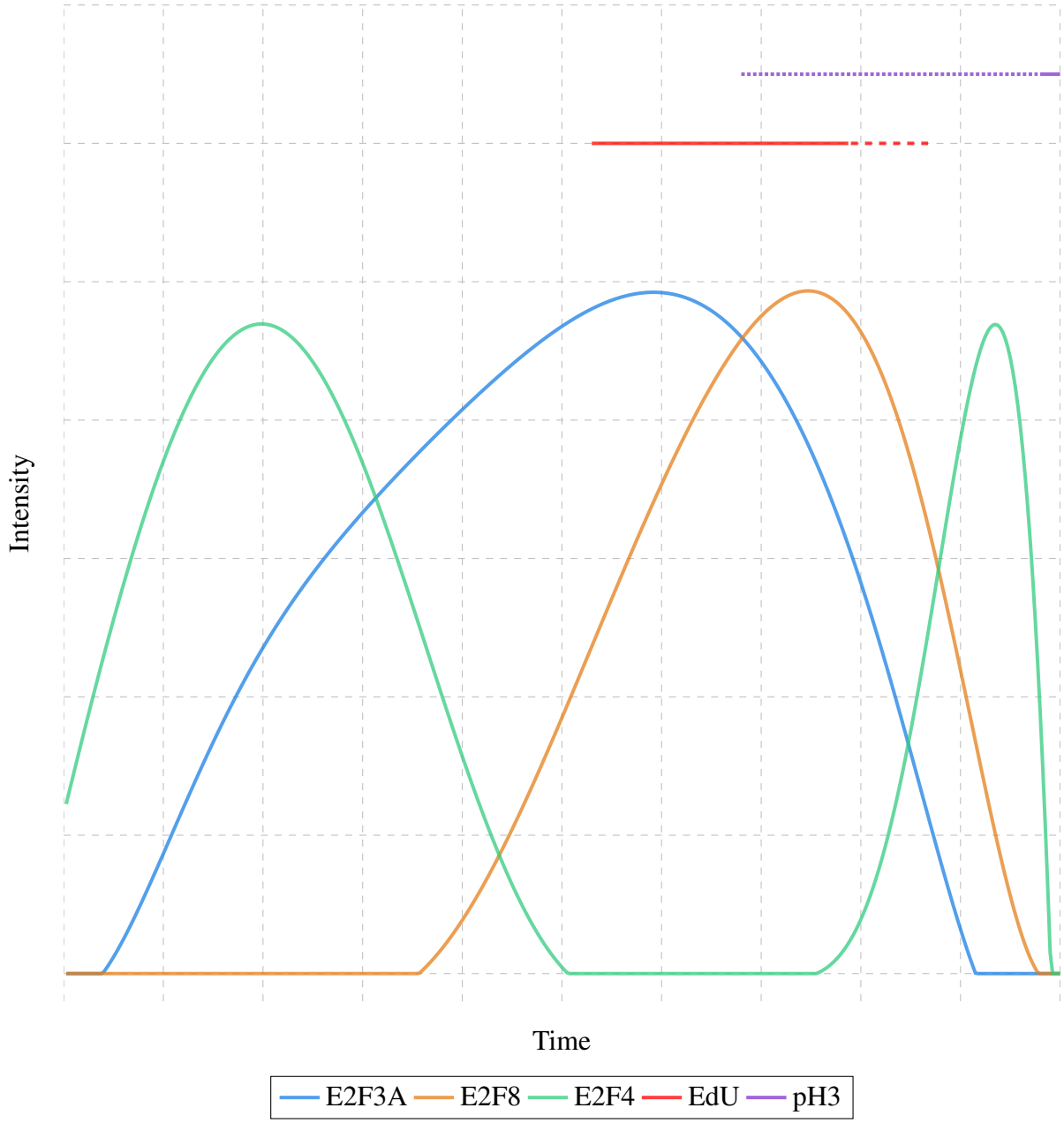


Figure 4: **Estimation of E2Fs accumulation over the cell cycle.** Temporal evolution of E2F3A, E2F8 and E2F4 protein accumulation, as well as EdU and pH3 patterns over the cell cycle in mouse intestinal epithelium.

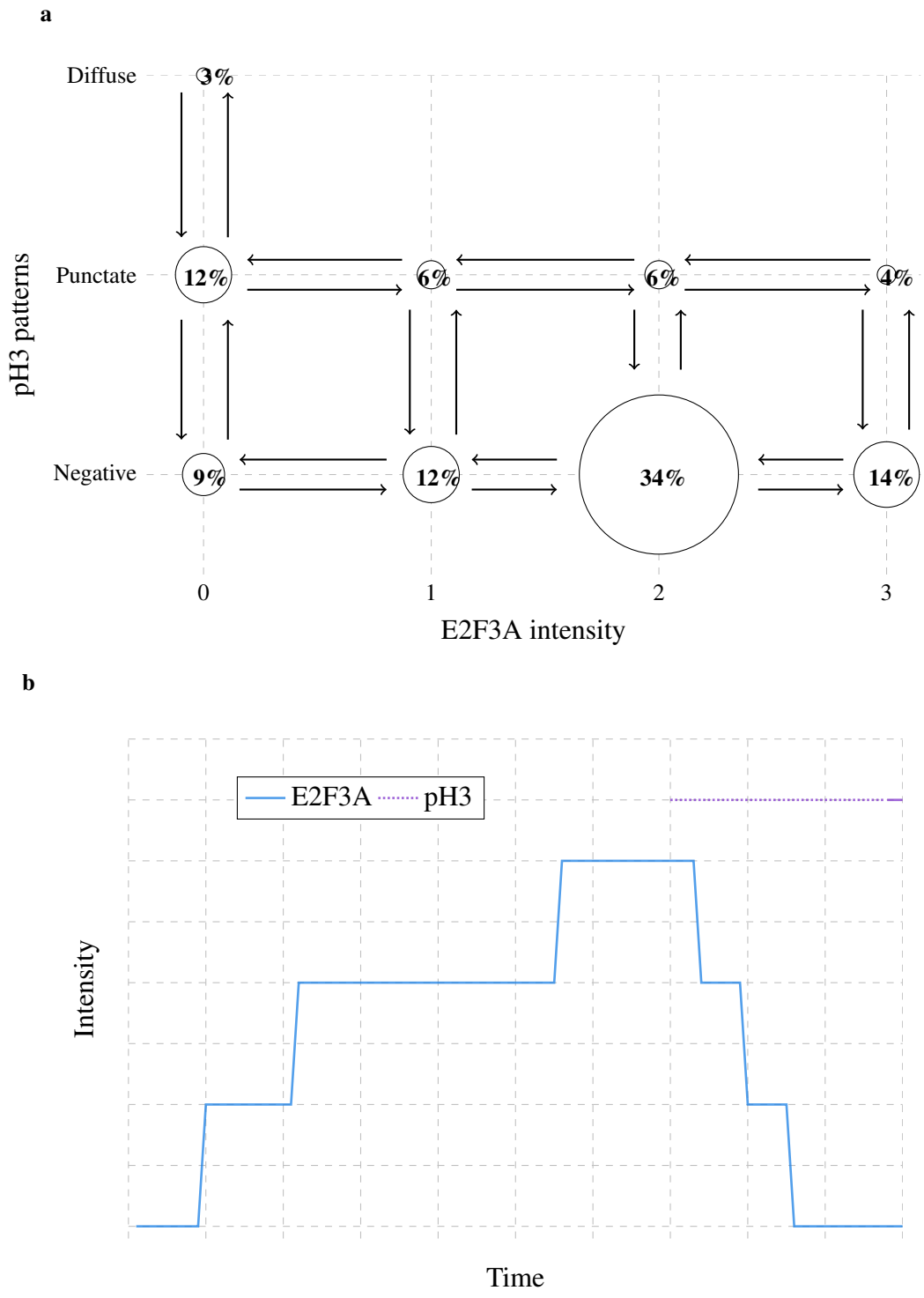


Figure 4 supplement 1: **Initialization of E2F3A and pH3.** **a** 2D histogram of E2F3A intensity and pH3 patterns. **b** Initialization of E2F3A and pH3 over time from the 2D histogram shown in **a**.

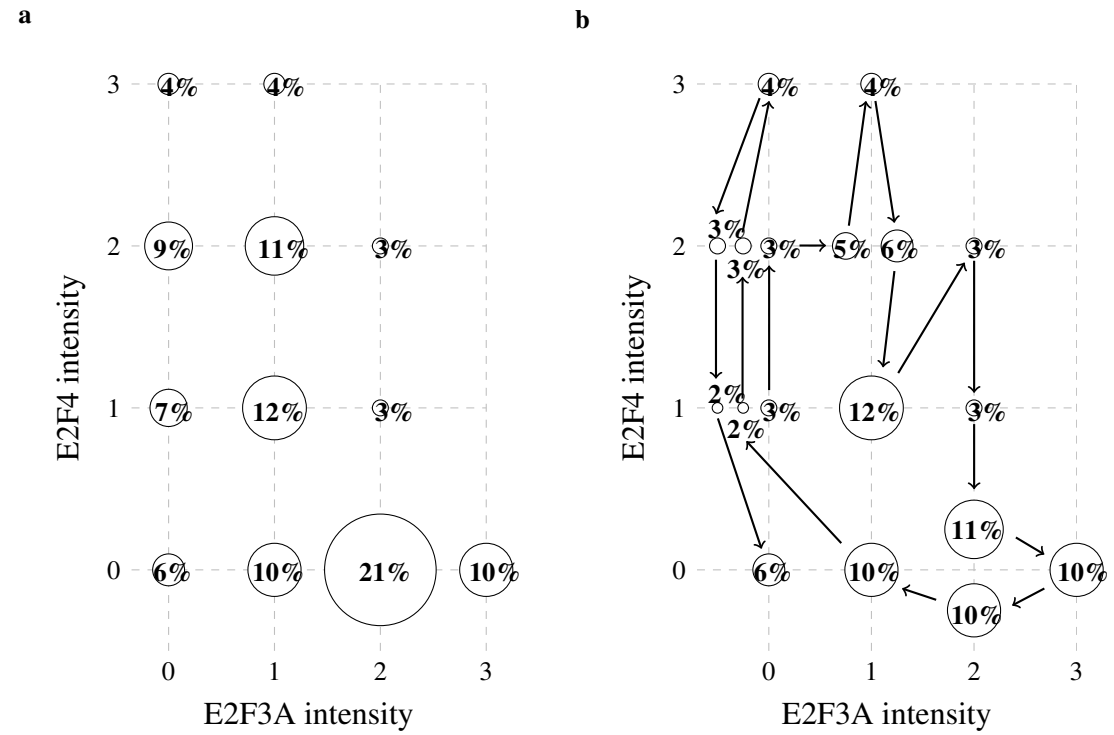


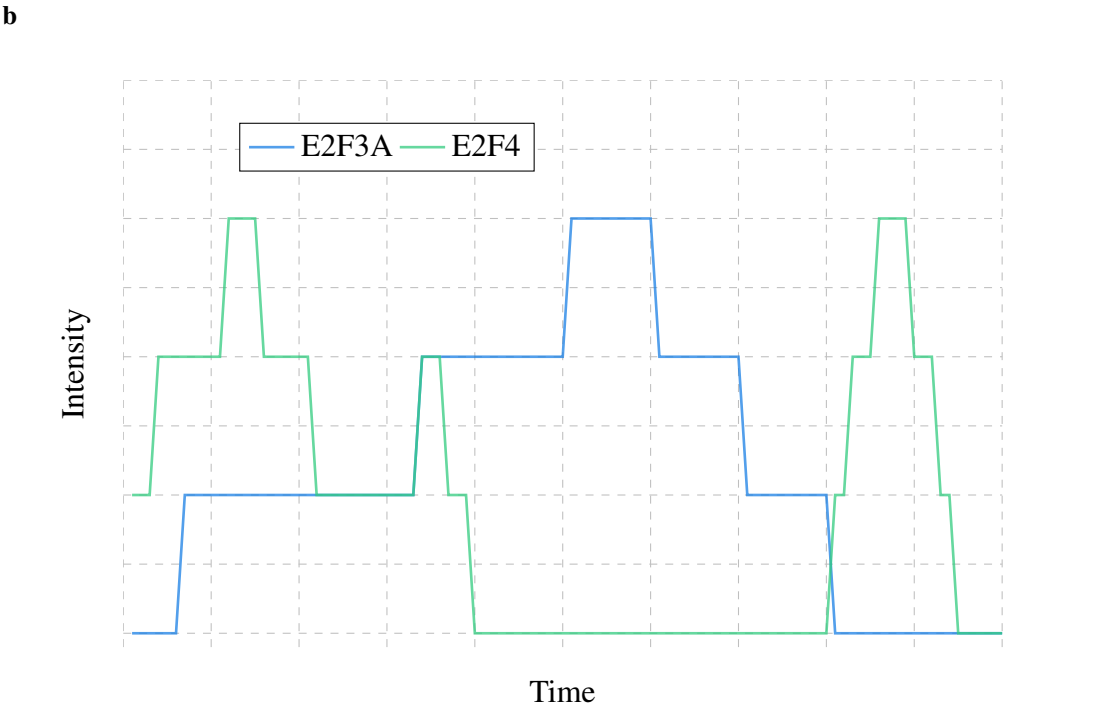


Figure 4 supplement 2: **Initialization of E2F3A and E2F4. a** 2D histogram of E2F3A and E2F4 intensity. **b** Modified 2D histogram of E2F3A and E2F4 intensity with vertex splitting and set of edges giving the minimum cost. **c** Initialization of E2F3A and E2F4 over time from the set of edges shown in **b**.

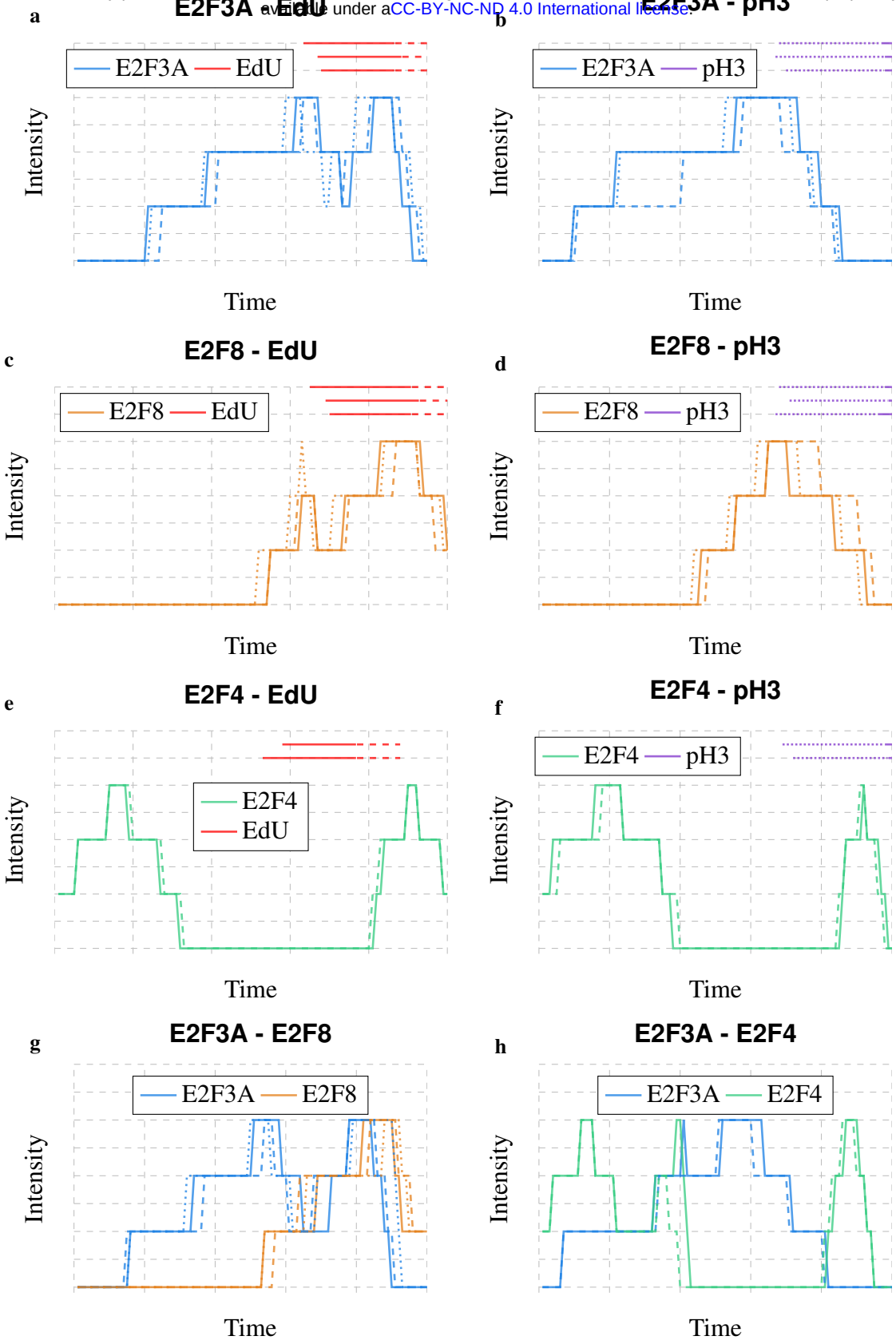


Figure 4 supplement 3: **Initialization of E2Fs with respect to EdU and pH3. a-b** Initialization of E2F3A with respect to **a** EdU (n=3) and **b** pH3 (n=3). **c-d** Initialization of E2F8 concentration with respect to **c** EdU (n=3) and **d** pH3 (n=3). **e-f** Initialization of E2F4 concentration with respect to **e** EdU (n=2) and **f** pH3 (n=2). **g-h** Initialization of E2F3A concentration with respect to **g** E2F8 (n=3) and **h** E2F4 (n=2). For all curves, the E2Fs intensity for the different mice are represented as curves with different line styles while EdU and pH3 are shown above the E2Fs curves, with solid lines corresponding to diffuse states and dashed lines corresponding to punctate states.

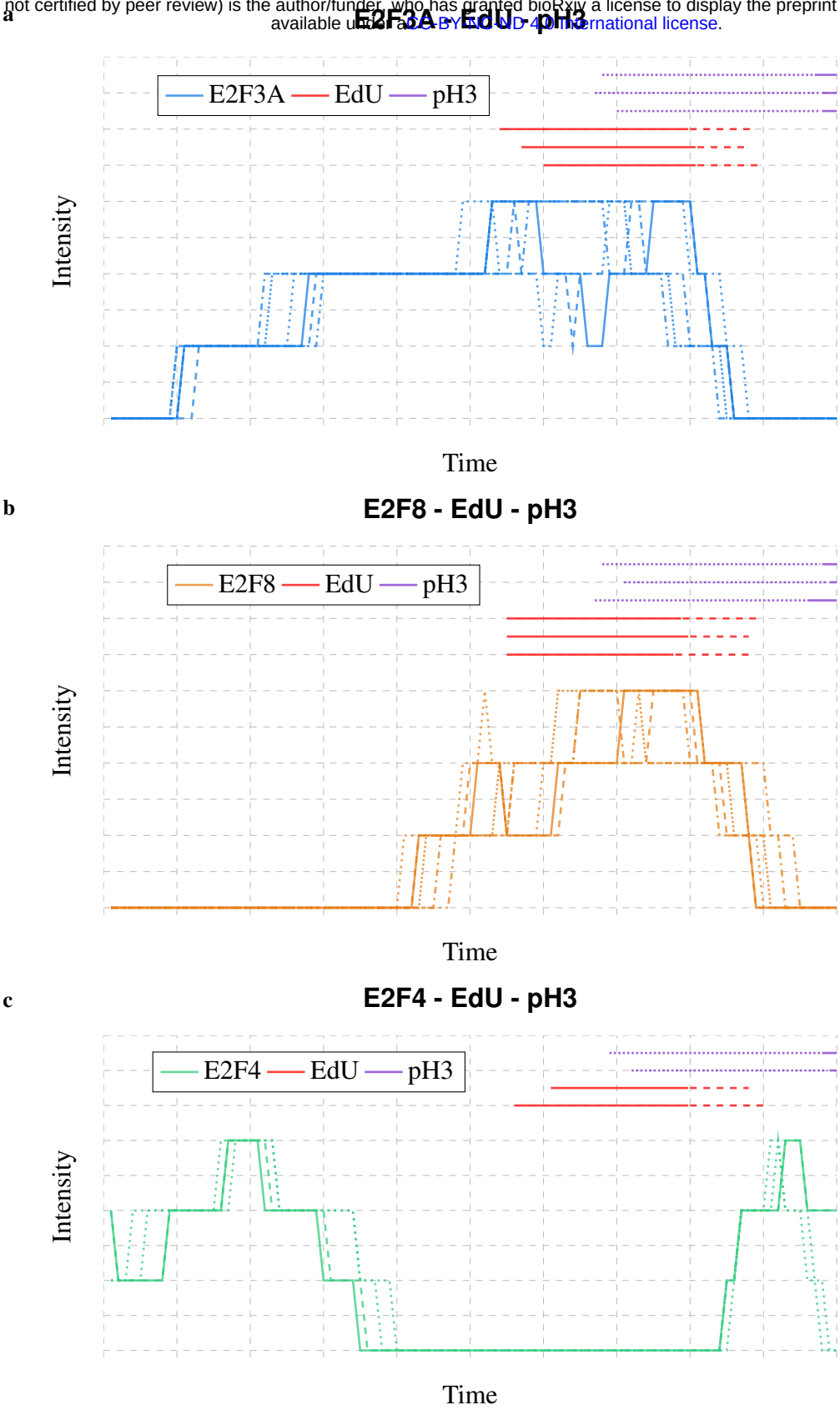


Figure 4 supplement 4: **Initialization of E2Fs evolution over the cell cycle. a** Temporal evolution of E2F3A over the cell cycle after registration between EdU and pH3 (n=6). **b** Temporal evolution of E2F8 over the cell cycle after registration between EdU and pH3 (n=6). **c** Temporal evolution of E2F4 over the cell cycle after registration between EdU and pH3 (n=4). For all curves, the E2Fs intensity for the different mice are represented as curves with different line styles while EdU and pH3 are shown above the E2Fs curves, with solid lines corresponding to diffuse states and dashed lines corresponding to punctate states.

developing pseudostratified epithelia (Grosse et al. 2011, Miyata 2008, Ueno et al. 2006). After applying QuantEv to each fluorescence marker used in this study, no statistical difference was observed between EdU diffuse and EdU punctate (Fig. 5 **b**). Notably, the EdU diffuse distribution peak was closer to the basement membrane than the EdU punctate distribution peak, which is consistent with the timing of early and late S-phase during the cell cycle (*i.e.* the EdU diffuse pattern appears in early-mid S whereas EdU punctate occurs in late S). Additionally, the basal-luminal distribution of E2F-expressing nuclei recapitulated the temporal expression of E2F during the cell cycle; E2F3A or E2F8 labeled nuclei predominated basally, with a more prominently basal E2F3A distribution, whereas E2F4-expressing nuclei accumulated mostly apically (Fig. 5 **c**). In addition, the E2F4 peak in G1 (Fig. 4, green curve) does not translate to a peak close to the basement membrane, suggesting that nuclei in G1 – early S are not differentially localized. Taken together, these results support the notion that nuclear location within the epithelium of the developing mouse intestine is correlated with cell cycle.

## DISCUSSION

This study demonstrates that the Mask R-CNN approach, coupled with transfer learning and data augmentation, can produce highly accurate nuclear segmentation of fluorescent images, even in a complex tissue such as the intestinal epithelium, by considering a small training dataset. Outstanding segmentation results are achieved for different imaging modalities, notably including widefield fluorescence microscopy, a ubiquitous imaging mode in cell biology research labs that produces challenging images of low sharpness and poor boundary definition. This is of major interest, as

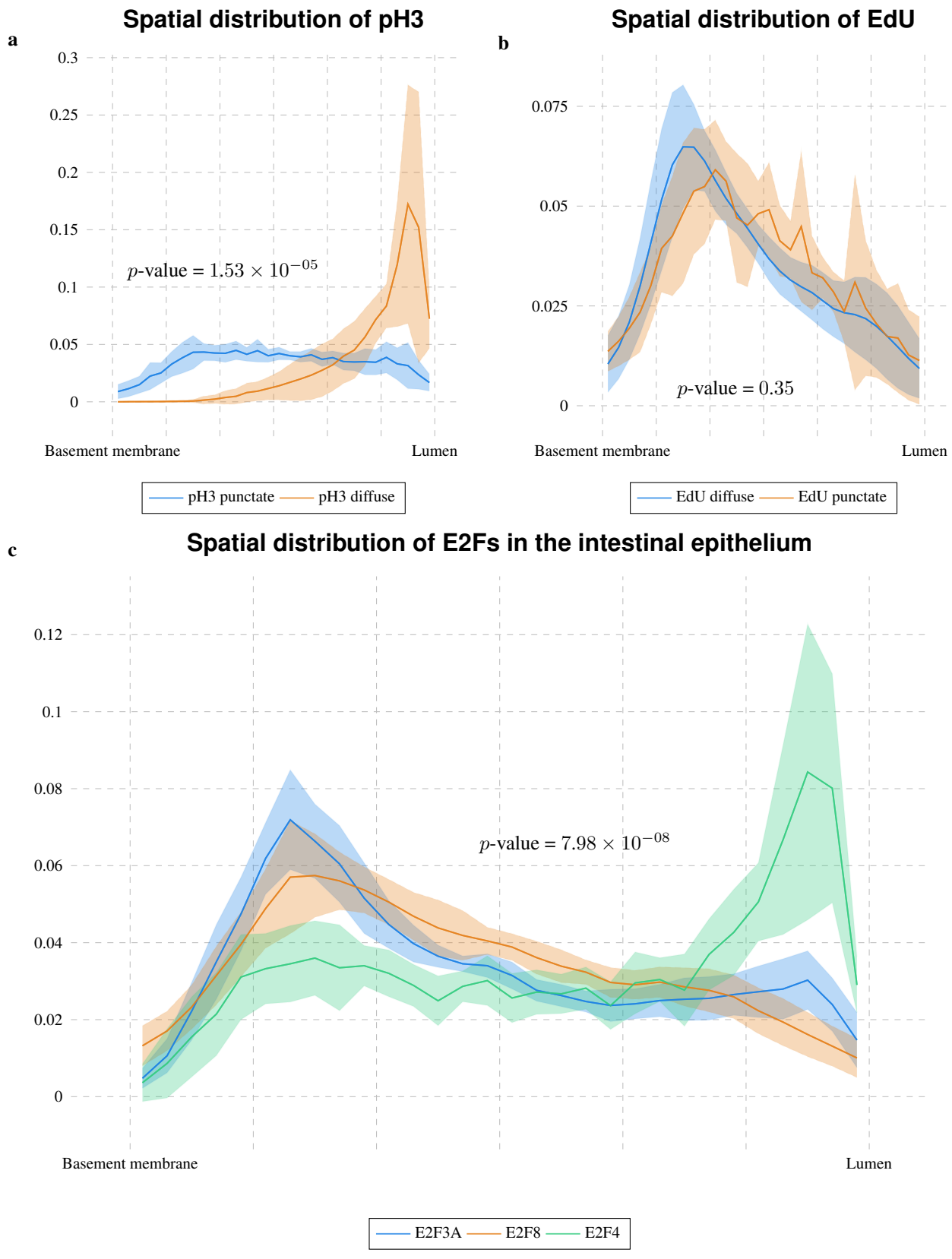


Figure 5: **Spatial distribution of pH3, EdU and E2Fs in the intestinal epithelium. a-c** Spatial distribution of pH3 **a**, EdU **b** and E2F3A, E2F8 and E2F4 **c** in the intestinal epithelium. The lines correspond to the average spatial distribution densities while the areas represent the standard error.

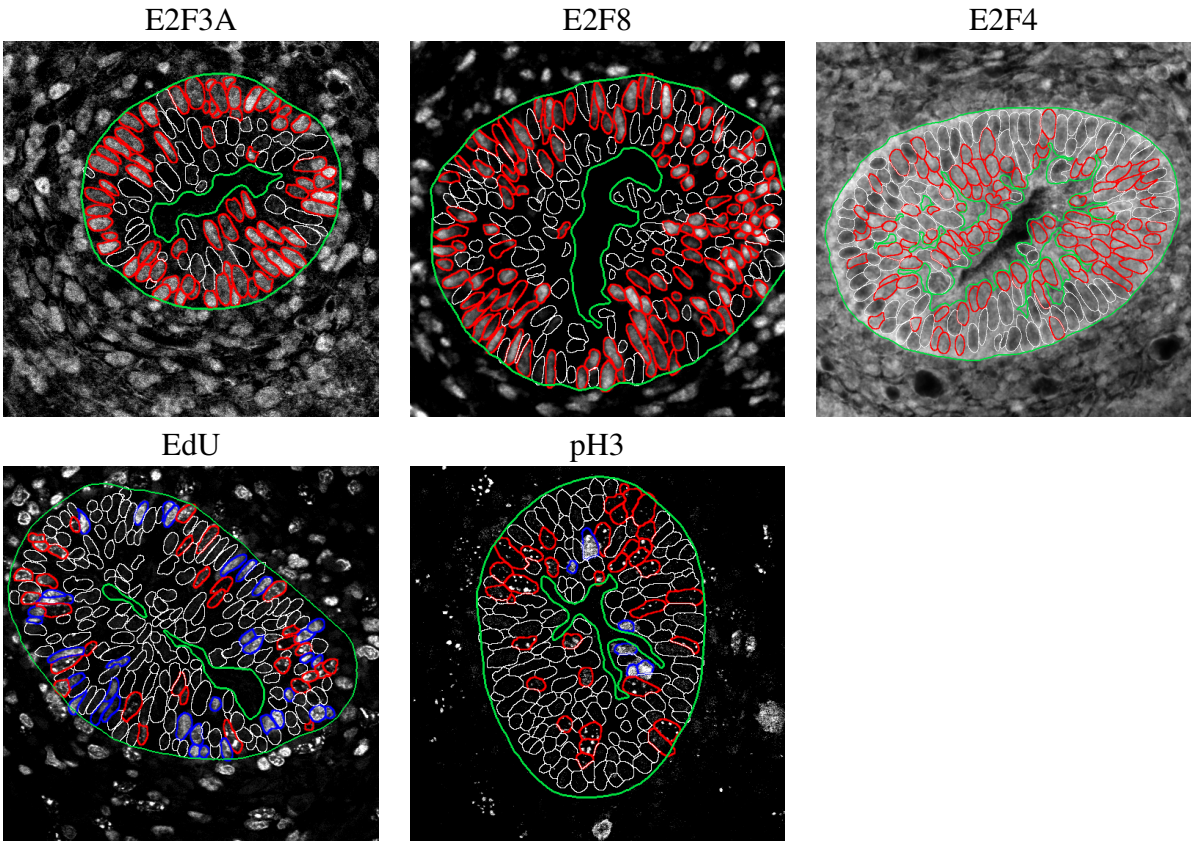


Figure 5 supplement 1: **Examples of the localization of pH3, EdU and E2Fs in the intestinal epithelium.** Images showing the localization of E2F3A positive (red), E2F8 positive (red), E2F4 positive (red), EdU diffuse (blue), EdU punctate (red), pH3 diffuse (blue), pH3 punctate (red), and negative (white) nuclei in the mouse intestinal epithelium. The outer green lines outline the basement membrane while the inner green lines delineate the lumen.

segmentation is a key task in image analysis of mammalian tissues where variability across tissue types is high and the number of modalities large and ever increasing. Therefore, the quest for comprehensive training datasets will be long and biology laboratories need efficient strategies to process their own images. In this context, the Inception-V3 approach also obtains satisfactory segmentation accuracy, but the computation time, especially for training, represents a major limitation. Though the U-Net approach has demonstrated its utility in many biomedical studies, it is unable to generalize the ability to segment nuclei when the images are acquired with different modalities.

Our results also attest to the superiority and efficiency of the deep learning approach for identifying the presence and state of nuclear markers. As the goal is to make a decision for each cell, the Inception-V3 architecture is well adapted to the task, computation time not being the issue that it is for nuclear segmentation. Considering pixel-based input patches improves performance if the training dataset is small. Moreover, transfer learning from nuclear segmentation improves marker identification. This is explained by the fact that image features that are suited for nuclear segmentation are also meaningful for identifying nuclear markers. This is an interesting observation, as the same strategy could be used in an n-steps pipeline analysis. Indeed, a deep learning classifier could be trained for the first analysis applied to a particular dataset, the resulting parameters used to initialize the classifier for the second analysis, and so on.

While deep learning approaches for both nuclear segmentation and nuclear marker identification show high accuracy, some level of discrepancy between desired and actual results is expected.

Thus, it is important to allow the user to correct the results if higher accuracy is required. This need for interactive post-processing of the results motivated us to design and implement the ImageJ plugin Annotater. This plugin can be used to annotate data from scratch or to perform corrections. While Annotater could be used to obtain perfect accuracy even without prior automated segmentation and marker identification, starting from a good estimate markedly speeds up the process. For instance, delineating the boundaries of all nuclei in an image of the intestinal epithelium may take a trained user 1-1.5 hours whereas any user can correct the results obtained with the Mask R-CNN approach in less than five minutes.

We present a novel and powerful method to estimate temporal phenomena using quantitative analysis of 2D still images. Specifically, we showed how the time-variant concentrations of intra-nuclear proteins can be qualitatively obtained from snapshot images of cell populations of reasonable size (for example, FFPE images of hundreds of epithelial cells as we analyzed in this study). Compared to alternative methods like single-cell analysis of individual living cells, the method we put forward here potentially allows easier and less expensive experimental designs for many applications in which dynamic protein expression information is required. In this particular case, a smart initialization based on biologically relevant assumptions coupled with a global optimization approach enabled estimation of E2F accumulation over the cell cycle.

Finally, we show that our approach is able to quantitatively demonstrate a correlation between nuclear location and cell cycle phase in the embryonic intestinal epithelium. These results emphasize the value of objective spatial analyses in tissues with complex architectural patterns

and its potential use for the assessment of cell polarity, cell cycle dynamics and other measurable structural compartmental relations within mammalian tissues.

## ACKNOWLEDGEMENTS

The Titan Xp used for this research was donated by the NVIDIA Corporation. This work was funded by a Chan Zuckerberg Initiative DAF grant to T.P. (2019-198009).

## AUTHOR CONTRIBUTIONS

M.C.C. performed widefield and confocal microscopy imaging. T.P. conceived and implemented the methods, processed and analyzed the data, and prepared figures. All authors assisted with data interpretation and manuscript review. T.P. wrote the manuscript with input from all authors.

## DECLARATION OF INTEREST

The authors declare no competing interests.

## METHODS AND MATERIALS

### Mouse models and care

The E2f4$^{myc/myc}$ and E2f8$^{myc/myc}$ were generated using standard homologous recombination cloning techniques as described in Cuitiño et al. (2019). E2f4$^{myc/myc}$, E2F8$^{myc/myc}$ and wild type controls

were maintained on a mixed background (FVB/NT, 129v/Sv, C57BL/6NT). Mouse usage and protocols were approved by the Institutional Animal Care and Use Committee at the Ohio State University and Medical University of South Carolina. Mice were housed under normal husbandry conditions (five or less animals per cage) in a vivarium with a 12-hour light/dark cycle. Tissues were collected from E13.5 intestinal epithelium.

**Immunostaining**

Immunostaining was performed on a Bond Rx (Leica) or Ventana discovery ultra (Roche) autostainer as per manufacturer's instructions as previously described (Campton et al. 2015, Pitarresi et al. 2016). Primary antibodies and dilutions used in this study were as follows: pH3-S10 (Millipore; 06-570, 1:250), E2f3a (Millipore; 05-551, 1:100) and Myc-tag (Cell Signaling Technology; 2278, 1:100). EdU staining was performed following the manufacturer's protocol (Life Technologies; C10337).

**Image acquisition**

Widefield micrographs were collected using a Nikon Eclipse Ni-U microscope with a DS-Qi2 camera and NIS-Elements Advanced Research software. Confocal micrographs were collected using the Olympus FV 1000 Filter Confocal system in the Campus Microscopy and Imaging Facility at the Ohio State University.

## Nuclei segmentation

The three deep learning approaches were coded in Python and used the Python libraries numpy (Van der Walt et al. 2011), tensorflow (Abadi et al. 2015), keras (Chollet 2015), scipy (Virtanen et al. 2020) and scikit-image (Van der Walt et al. 2014). The code with the parameters used to train and process all experiments presented in this manuscript is available at `https://github.com/tpecot/NucleiSegmentationAndMarkerIDentification/tree/master/`.

**Training dataset** The training dataset for nuclei segmentation consisted of twelve confocal and forty-five widefield 512 x 512 images annotated by a moderately-skilled researcher. For U-Net and Mask R-CNN approaches, nine confocal and thirty-seven of the widefield images were used for training while the other three confocal and eight widefield images were used for validation. For the Inception-V3 approach, ninety percent of image patches were used for training and ten percent of image patches were used for validation.

**U-Net** As the U-Net approach estimates a class at each pixel, three classes were defined to allow separating nuclei as proposed in Van Valen et al. (2016): inner nuclei, nuclei contours and background. To facilitate nuclei separation, the nuclei contours in the training dataset were dilated (Van Valen et al. 2016). To reduce memory usage and limit over-fitting, the imaging field for images in the training dataset was set to 256 x 256 by randomly cropping the 512 x 512 input images. These cropped images were then normalized by dividing the intensity at each pixel by the median intensity over the image and by subtracting at each pixel the average intensity of a 64 x 64 neighborhood around it. A root mean square prop was used to estimate the parameters of the

deep convolutional neural network by minimizing a weighted cross entropy loss to handle class imbalance for 10 epochs. The weights associated with each class were defined from the training dataset as their inverse proportion. A data augmentation to increase the training dataset by a factor of 100 was processed before normalization with the imgaug python library (Jung et al. 2020) and included flipping, rotation, shearing, blurring, sharpness and brightness modifications, noise addition, intensity inversion and contrast modifications. Of note, the optimal image augmentation parameters were different for confocal and widefield images: a better performance was obtained with low value parameters for confocal images and high value parameters for widefield images. This suggests that complex data (widefield images) need to be more perturbed than less complex data (confocal images) to improve U-Net's ability to accurately segment nuclei. This also explains why the nuclei segmentation results are degraded when confocal and widefield images are pooled together in the training dataset.

**Inception-V3** The same three classes were defined and the nuclei contours were dilated for the Inception-V3 approach as for the U-Net approach. The imaging field was set to 65 x 65 pixel image patches, large enough to include at least one nucleus as suggested in Van Valen et al. (2016). For each image patch, only the class of the central pixel was trained or processed. The training images were normalized the same way as for the U-Net approach, *i.e.* dividing the intensity at each pixel by the median intensity over the image and subtracting at each pixel the average intensity in a 65 x 65 neighborhood around it. To obtain a balanced training dataset, the same number of input image patches were defined for each class. A stochastic gradient descent was used to estimate the parameters of the deep convolutional neural network by minimizing a categorical cross entropy for

15 epochs. A modification of the input image patches was processed after normalization with the imgaug python library (Jung et al. 2020) and included the same image transformations that were used for the U-Net approach.

**U-Net and Inception-V3 post-processing** For both U-Net and Inception-V3 approaches, nuclei were obtained by subtracting the nuclei contours from the inner nuclei. Let us define $\mathbf{S}_c = \{S_c(x)\}_{x\in\Omega}$ where $S_c(x)$ denotes the nuclei contour score obtained with the U-Net or the Inception-V3 approach at pixel $x$, and $\Omega$ is the regular grid of pixels in the image. Similarly, we define $\mathbf{S}_n = \{S_n(x)\}_{x\in\Omega}$ the inner nuclei score at each pixel $x$. The nuclei component $\mathbf{N} = \{N(x)\}_{x\in\Omega}$ is defined as:

$$N(x) = S_n(x) - S_c(x). \tag{1}$$

This nuclei component is then thresholded to define a binary image $\mathbf{N}_b$:

$$N_b(x) = \begin{cases} 1 & \text{if } N(x) > 0, \\ 0 & \text{otherwise.} \end{cases} \tag{2}$$

The individual nuclei are defined as the connected components of the binary image $\mathbf{N}_b$. This leads to an under segmentation when contours between touching nuclei are not well estimated. Consequently, we propose to apply the watershed algorithm (Vincent & Soille 1991) on the nuclei component $\mathbf{N}$ and to take advantage of the nuclei contour score $\mathbf{S}_c$ obtained from the U-Net or Inception-V3 output to refine the segmentation. Let us define $\mathbf{W} = \{W(x)\}_{i\in\Omega}$ the result of the watershed algorithm applied to the inverse intensity of the nuclei component $\mathbf{N}$ prealably convolved with a Gaussian filter of kernel size 2.5 for U-Net and 3.5 for Inception-V3. From $\mathbf{W}$, a set of K new nuclei separations $\{\mathcal{S}(k)\}_{k=1,\dots,K}$ is obtained. A score $\mathbf{S}_w = \{S_w(k)\}_{k=1,\dots,K}$ is defined

for each new separation $\mathcal{S}(k)$ as follows:

$$S_w(k) = \sum_{x \in \mathcal{S}(k)} S_c(x) - S_n(x). \tag{3}$$

All nuclei separations $\mathcal{S}(k)$ such that $S_w(k) > 0$ are used to separate the nuclei obtained as the connected components of the binary image $\mathbf{N}_b$.

**Mask R-CNN** Version 2.1 of Mask R-CNN (He et al. 2017) was used in this study. The backbone network was defined as the Resnet-101 deep convolutional neural network (He et al. 2016). We used the code in Hollandi et al. (2020) to define the only class in this study, *i.e.* the nuclei. A data augmentation to increase the training dataset by a factor of 100 was processed before normalization with the imgaug python library (Jung et al. 2020) and included resizing, cropping, flipping, rotation, shearing, blurring, sharpness and brightness modifications, noise addition, intensity inversion and contrast modifications. Transfer learning with fine-tuning from a network trained on the coco dataset (Lin et al. 2014) was also applied. In the first epoch, only the region proposal network, the classifier and mask heads were trained. The whole network was then trained for the next three epochs.

**Evaluation** As proposed by Caicedo *et al.* (2019), we used the F1 score with respect to the Intersection over Union ($IoU$) to compare the three deep learning approaches. We evaluated three different images for both confocal and widefield modalities annotated by a pathologist (a high-skilled researcher). Let $\mathbf{O}_{GT} = \{O_{GT}(e)\}_{e=1,\dots,n}$ be the set of $n$ ground truth nuclei, as defined by the pathologist, and $\mathbf{O}_E = \{O_E(e)\}_{e=1,\dots,m}$ be the set of $m$ estimated nuclei with a deep learning approach. The $IoU$ defined between the truth nucleus $O_{GT}(e_1)$ and the estimated nucleus $O_E(e_2)$

was defined as:

$$IoU(O_{GT}(e_1), O_E(e_2)) = \frac{O_{GT}(e_1) \cap O_E(e_2)}{O_{GT}(e_1) \cup O_E(e_2)}. \tag{4}$$

An $IoU(O_{GT}(e_1), O_E(e_2))$ equal to $0$ implies that $O_{GT}(e_1)$ and $O_E(e_2)$ do not share any pixel while an $IoU(O_{GT}(e_1), O_E(e_2))$ equal to $1$ means that $O_{GT}(e_1)$ and $O_E(e_2)$ are identical. An $IoU(O_{GT}(e_1), O_E(e_2))$ equal to $0.5$ ensures that $IoU(O_{GT}(e_1), O_E(e_3)) < 0.5$, $\forall e_3 \neq e_2$ as a nucleus cannot share half of its area with more than one nucleus. Consequently, the F1 score for a given $IoU$ threshold $t > 0.5$ can be defined as:

$$F1(t) = \frac{2 \times TP(t)}{2 \times TP(t) + FN(t) + FP(t)}, \tag{5}$$

where

$$TP(t) = \sum_{e_1 \in \{1,\ldots,n\}, e_2 \in \{1,\ldots,m\}} \mathbb{1}\left(IoU(O_{GT}(e_1), O_E(e_2)) > t\right), \tag{6}$$

$$FN(t) = \sum_{e_1 \in \{1,\ldots,n\}} \mathbb{1}\left(IoU(O_{GT}(e_1), O_E(e_2)) < t\right), \forall e_2 \in \{1,\ldots,m\}, \tag{7}$$

$$FP(t) = \sum_{e_2 \in \{1,\ldots,m\}} \mathbb{1}\left(IoU(O_{GT}(e_1), O_E(e_2)) < t\right), \forall e_1 \in \{1,\ldots,n\}, \tag{8}$$

and

$$\mathbb{1}(\mathcal{C}) = \begin{cases} 1 \text{ if } \mathcal{C} \text{ is true,} \\ 0 \text{ otherwise.} \end{cases} \tag{9}$$

With a threshold $t = 0.5$, this metric gives the accuracy of a method to identify the correct number of nuclei, while with thresholds in the range $0.5 - 1$, it evaluates the localization accuracy of the identified nuclear contours.

## Marker identification

**Training dataset** As Mask R-CNN and U-Net are not suited for the task, the Inception-V3 method was used for marker identification. The training dataset consisted of eight confocal images for E2F3A, five confocal images for E2F8, four confocal images for EdU, three confocal images for pH3, twenty-one widefield images for E2F3A and fifteen widefield images for E2F8, E2F4, EdU and pH3, all annotated by a moderately-skilled researcher. Ninety percent of image patches were used for training and ten percent for validation. Two training strategies were designed to define the input image patches: The first only considered image patches centered at each nucleus center, while the second strategy included images patches centered at each pixel in the segmented nuclei, drastically increasing the amount of training data.

**Inception-V3** Two classes (positive and negative) were defined for the E2Fs, while three classes (diffuse, punctate and negative) were defined for EdU and pH3. As for nuclei segmentation, the imaging field was set to 65 x 65 pixel image patches to ensure inclusion of at least one entire nucleus. The training image patches were normalized by subtracting at each pixel the average intensity in a 65 x 65 neighborhood. Intensities were not divided by the median intensity over the image as they were for nuclei segmentation because the median can be equal to zero for sparse markers such as pH3. To obtain a balanced training dataset, the same number of input image patches was defined for each class. A stochastic gradient descent was used to estimate the parameters of the deep convolutional neural network by minimizing a categorical cross entropy for 10 epochs. To increase the size of the nuclei-based training dataset 100-fold, a data augmentation that included

flipping, rotation, shearing, blurring, sharpness and brightness modifications, noise addition, inversion and contrast modifications was performed after normalization with the imgaug python library (Jung et al. 2020). A transfer learning with fine-tuning from the Inception-V3 network trained for nuclei segmentation on confocal and widefield images was performed on the pixel-based training dataset. In the first epoch, only the last layer of the network was trained. The whole network was then trained for the next five epochs.

**Thresholding** Marker identification was also evaluated when thresholding marker intensity in the nuclei with the ImageJ plugin Annotater. For E2Fs, nuclei with more than thirty-five percent of their area above a manually defined threshold were considered positive. For EdU, nuclei with more that seventy percent of their area above a manually defined threshold were considered diffuse, while nuclei with more than fifteen percent but less than seventy percent of their area above the same threshold were considered punctate. For pH3, nuclei with more that ninety percent of their area above a manually defined threshold were considered diffuse, while nuclei with more than ten percent but less than ninety percent of their area above the same threshold were considered punctate.

**Evaluation** Evaluation was performed using three confocal and three widefield images for E2F3A and E2F8, using three widefield images for E2F4, and using two confocal and three widefield images for EdU and pH3. All the images used for evaluation were annotated by a moderately-skilled researcher. The nuclei locations were known and only their class (positive/negative or diffuse/punctate/negative) was evaluated. Let $\mathbf{C}_{GT} = \{C_{GT}(e)\}_{e=1,\dots,n}$ be the ground truth class

for the $n$ nuclei and let $\mathbf{C}_E = \{C_E(e)\}_{e=1,\ldots,n}$ be the estimated class for each nucleus. Class estimation accuracy is then defined as:

$$\text{accuracy} = \frac{TP}{n}, \tag{10}$$

where

$$TP = \sum_{e=1}^{n} \mathbb{1}\left(C_{GT}(e) = C_E(e)\right). \tag{11}$$

**ImageJ plugin Annotater**

We developed the plugin entitled *Annotater* to draw nuclear contours manually to define training datasets and to interactively correct deep learning-based nuclei segmentations. This plugin also provides for manual characterization of markers associated with nuclei and a thresholding tool for specifying an intensity threshold and the proportion of pixels in a nucleus above that threshold that defines a positive nucleus. Finally, Annotater can generate images in which segmented nuclei and marker characterization are overlaid on the input image and can extract nuclear features as defined in the *Set Measurements* window in ImageJ. The java code of the plugin is available at `https://github.com/tpecot/Annotater/tree/master/src/main/java/edu/musc/tsl` and the plugin is available at `https://github.com/tpecot/Annotater`. Video tutorials showing how to use the plugin are available at `https://github.com/tpecot/Annotater`.

## E2Fs accumulation over the cell cycle from 2D still images

**Data** Several levels of intensity for E2Fs were required to estimate fluorescence evolution over the cell cycle. To minimize the effects of noise while still being able to observe fluorescence fluctuations, we decided to define four levels of intensity. First, the negative cells were assigned an intensity equal to 0. Then, for each individual image, the average fluorescence intensity for each positive cell was processed and the range of average intensities from the lowest to the highest was binned into three to define levels 1 to 3. The state of EdU and pH3 markers for each nucleus was already known from the marker identification as being diffuse, punctate or negative. More formally, let us define $I_e^{\text{Ch1}} \in \{0, 1, 2, 3\}$ the average intensity in Ch1 for nucleus $e \in \{1, \dots, n\}$ in an image with $n$ nuclei, where Ch1 is a channel corresponding to E2F3A, E2F8 or E2F4. Similarly, $I_e^{\text{Ch2}} \in \{0, 1, 2, 3\}$ is the average intensity in Ch2 for nucleus $e$ if Ch2 is E2F4 or E2F8 and $I_e^{\text{Ch2}} \in \{0, \text{diffuse}, \text{punctate}\}$ is the state of nucleus $e$ if Ch2 is EdU or pH3. The estimation of fluorescence accumulation over the cell cycle is performed in 3 steps: i) initialization, ii) registration with respect to cell cycle, iii) global optimization.

**Initialization** Let us define $h(I^{\text{Ch1}} = u_1, I^{\text{Ch2}} = u_2)$ the number of nuclei for which the intensity in Ch1 is equal to $u_1$ and the intensity or state in Ch2 is equal to $u_2$:

$$h\left(I^{\text{Ch1}} = u_1, I^{\text{Ch2}} = u_2\right) = \sum_{e=1}^{n} \mathbb{1}\left(I_e^{\text{Ch1}} = u_1\right) \mathbb{1}\left(I_e^{\text{Ch2}} = u_2\right). \tag{12}$$

We can now define $\mathbf{H} = \{H(I^{\text{Ch1}} = u_1, I^{\text{Ch2}} = u_2)\}_{u_1=\{0,1,2,3\}, u_2=\{0,1,2,3\} \text{ or } u_2=\{0,\text{diffuse},\text{punctate}\}}$ the 2D intensity histogram as follows:

$$H\left(I^{\text{Ch1}} = u_1, I^{\text{Ch2}} = u_2\right) = \frac{h\left(I^{\text{Ch1}} = u_1, I^{\text{Ch2}} = u_2\right)}{n}. \tag{13}$$

An example of a 2D histogram of E2F3A intensity and pH3 patterns is shown in Fig. 4 supp. 1 **a**. According to our first and second assumptions, *i.e.* time depends on the proportion of cells in the images and temporal evolution of protein accumulation is similar in all observed cells, 2D intensity histograms provide the proportion of nuclei for combination of E2Fs intensities or E2Fs intensity and EdU/pH3 patterns. For example, in the image considered to build the histogram shown in Fig. 4 supp. 1 **a**, thirty-four percent of nuclei have an intensity of 2 for E2F3A and are negative for pH3. Combining these proportions allows to define the evolution of the intensity/state of the channels over the cell cycle. We propose to initialize the evolution of fluorescence over the cell cycle through a graph optimization procedure. Let us define a graph $\mathcal{G}(\mathcal{E},\mathcal{V})$ with $|\mathcal{V}|$ vertices corresponding to the different non-zero proportions of markers from a 2D histogram and $|\mathcal{E}|$ edges between neighbor vertices in the same histogram. For instance, in Fig. 4 supp. 1 **a**, there are nine vertices $\{\mathcal{V}_{E2F3A=0,pH3=\text{negative}}, \mathcal{V}_{E2F3A=1,pH3=\text{negative}}, \ldots, \mathcal{V}_{E2F3A=0,pH3=\text{diffuse}}\}$ represented as circles and twenty-two edges $\{\mathcal{E}(\mathcal{V}_{E2F3A=0,pH3=\text{negative}} \rightarrow \mathcal{V}_{E2F3A=1,pH3=\text{negative}}), \ldots, \mathcal{E}(\mathcal{V}_{E2F3A=0,pH3=\text{diffuse}} \rightarrow \mathcal{V}_{E2F3A=0,pH3=\text{punctate}})\}$ represented as unidirectional arrows. A cost $\mathcal{P}(\mathcal{E}(\mathcal{V}_{v_1},\mathcal{V}_{v_2}))$ is then assigned to each edge. From Cuitiño et al. (2019), we know that EdU is diffuse during the first half of S phase and then punctate during the second half of S phase. It implies that:

$$\begin{aligned}
\mathcal{P}(\mathcal{E}(\mathcal{V}_{G=u,EdU=\text{negative}}, \mathcal{V}_{G=u,EdU=\text{diffuse}})) &= 0,\\
\mathcal{P}(\mathcal{E}(\mathcal{V}_{G=u,EdU=\text{diffuse}}, \mathcal{V}_{G=u,EdU=\text{punctate}})) &= 0,\\
\mathcal{P}(\mathcal{E}(\mathcal{V}_{G=u,EdU=\text{punctate}}, \mathcal{V}_{G=u,EdU=\text{negative}})) &= 0,
\end{aligned} \tag{14}$$

while

$$\begin{aligned}
\mathcal{P}(\mathcal{E}(\mathcal{V}_{G=u,EdU=\text{diffuse}}, \mathcal{V}_{G=u,EdU=\text{negative}})) &= \infty, \\
\mathcal{P}(\mathcal{E}(\mathcal{V}_{G=u,EdU=\text{punctate}}, \mathcal{V}_{G=u,EdU=\text{diffuse}})) &= \infty, \\
\mathcal{P}(\mathcal{E}(\mathcal{V}_{G=u,EdU=\text{negative}}, \mathcal{V}_{G=u,EdU=\text{punctate}})) &= \infty,
\end{aligned} \tag{15}$$

where $G \in \{E2F3A, E2F8, E2F4\}$ and $u \in \{0, 1, 2, 3\}$. From Cuitiño et al. (2019), we also know that pH3 is first punctate during the second half of S phase and G2 and then diffuse during mitosis, so

$$\begin{aligned}
\mathcal{P}(\mathcal{E}(\mathcal{V}_{G=u,pH3=\text{negative}}, \mathcal{V}_{G=u,pH3=\text{punctate}})) &= 0, \\
\mathcal{P}(\mathcal{E}(\mathcal{V}_{G=u,pH3=\text{punctate}}, \mathcal{V}_{G=u,pH3=\text{diffuse}})) &= 0, \\
\mathcal{P}(\mathcal{E}(\mathcal{V}_{G=u,pH3=\text{diffuse}}, \mathcal{V}_{G=u,pH3=\text{negative}})) &= 0, \\
\mathcal{P}(\mathcal{E}(\mathcal{V}_{G=u,pH3=\text{punctate}}, \mathcal{V}_{G=u,pH3=\text{negative}})) &= \infty, \\
\mathcal{P}(\mathcal{E}(\mathcal{V}_{G=u,pH3=\text{diffuse}}, \mathcal{V}_{G=u,pH3=\text{punctate}})) &= \infty, \\
\mathcal{P}(\mathcal{E}(\mathcal{V}_{G=u,pH3=\text{negative}}, \mathcal{V}_{G=u,pH3=\text{diffuse}})) &= \infty,
\end{aligned} \tag{16}$$

where $G \in \{E2F3A, E2F8, E2F4\}$ and $u \in \{0, 1, 2, 3\}$. Finally, the evolution of E2Fs intensity needs to verify our third assumption, *i.e.* concentrations of E2Fs are concave downward parabolas, which explains why edges exist only between neighboring vertices in the 2D histograms:

$$\mathcal{P}(\mathcal{E}(\mathcal{V}_{G=u_1,M=s}, \mathcal{V}_{G=u_2,M=s})) = \begin{cases} 0 \text{ if } |u_1 - u_2| = 1, \\ \infty \text{ otherwise,} \end{cases} \tag{17}$$

where $G \in \{E2F3A, E2F8, E2F4\}$, $u_1 \in \{0, 1, 2, 3\}$, $u_2 \in \{0, 1, 2, 3\}$, $M \in \{\text{EdU,pH3}\}$ and $s \in \{\text{negative, punctate,diffuse}\}$. The evolution of the fluorescence is initialized as the sequence

of edges that goes through all vertices with a minimum cost. For instance, the only sequence of edges with a cost equal to 0 in the 2D histogram shown in Fig. 4 supp. 1 **a** is $\{\mathcal{V}_{E2F3A=0,pH3=\text{negative}}, \mathcal{V}_{E2F3A=1,pH3=\text{negative}}, \mathcal{V}_{E2F3A=2,pH3=\text{negative}}, \mathcal{V}_{E2F3A=3,pH3=\text{negative}}, \mathcal{V}_{E2F3A=3,pH3=\text{punctate}}, \mathcal{V}_{E2F3A=2,pH3=\text{punctate}}, \mathcal{V}_{E2F3A=1,pH3=\text{punctate}}, \mathcal{V}_{E2F3A=0,pH3=\text{punctate}}, \mathcal{V}_{E2F3A=0,pH3=\text{diffuse}}\}$. This sequence corresponds to the evolution of E2F3A and pH3 shown in Fig. 4 supp. 1 **b**.

We know that E2F4 shows two waves of expression over the cell cycle (Cuitiño et al. 2019), but a sequence of edges over a 2D histogram cannot reflect two downward parabolas. Consequently, splitting vertex(ices) is necessary. A cost of 1 is associated to each vertex splitting and added to the total cost. The split vertices give rise to multiple vertices containing equal proportion. For combinations of E2Fs with EdU as well as combinations of two different E2Fs, vertex splitting can also be required and may lead to E2Fs evolutions that do not look exactly like downward parabolas. This phenomenon arises from slight errors in nuclear intensity measurements, most likely due to image noise. A 2D histogram for the combination of E2F3A and E2F4 is shown in Fig. 4 supp. 2 **a**, the sequence of edges over this histogram for which vertices were split is shown in Fig. 4 supp. 2 **b** and the corresponding evolution of E2F3A and E2F4 is shown in Fig. 4 supp. 2 **c**.

By applying this cost minimization to all images, initializations for the eight different combinations of markers and averaged for each mouse are obtained. These initializations are shown in

Fig. 4 supp. 3. From these initializations, eight couples of marker sequences are defined:

$$\begin{aligned}
&\left\{{}^{\text{init}}X_i^{EdU-E2F3A}(c),\ {}^{\text{init}}X_i^{E2F3A-EdU}(c)\right\}_{c=1,\dots,B},\left\{{}^{\text{init}}X_i^{pH3-E2F3A}(c),\ {}^{\text{init}}X_i^{E2F3A-pH3}(c)\right\}_{c=1,\dots,B},\\
&\left\{{}^{\text{init}}X_i^{EdU-E2F8}(c),\ {}^{\text{init}}X_i^{E2F8-EdU}(c)\right\}_{c=1,\dots,B},\left\{{}^{\text{init}}X_i^{pH3-E2F8}(c),\ {}^{\text{init}}X_i^{E2F8-pH3}(c)\right\}_{c=1,\dots,B},\\
&\left\{{}^{\text{init}}X_i^{EdU-E2F4}(c),\ {}^{\text{init}}X_i^{E2F4-EdU}(c)\right\}_{c=1,\dots,B},\left\{{}^{\text{init}}X_i^{pH3-E2F4}(c),\ {}^{\text{init}}X_i^{E2F4-pH3}(c)\right\}_{c=1,\dots,B},\\
&\left\{{}^{\text{init}}X_i^{E2F3A-E2F8}(c),\ {}^{\text{init}}X_i^{E2F8-E2F3A}(c)\right\}_{c=1,\dots,B},\left\{{}^{\text{init}}X_i^{E2F3A-E2F4}(c),\ {}^{\text{init}}X_i^{E2F4-E2F3A}(c)\right\}_{c=1,\dots,B},
\end{aligned} \tag{18}$$

where ${}^{\text{init}}X_i^{M1-M2}(c)$ provides the level of fluorescence or pattern for marker $M1 \in \{E2F3A, E2F8, E2F4, EdU, pH3\}$ when combined with marker $M2 \in \{E2F3A, E2F8, E2F4, EdU, pH3\}$ for mouse $i$ at time $c$, $M1 \neq M2$, and $B$ is the number of time bins used to quantize the cell cycle: 100 bins in practice. The goal is to estimate the sequence for each of these couples of combinations.

**Registration** As EdU and pH3 expression patterns with respect to the cell cycle are known, E2Fs are first registered with respect to these two markers. We know that pH3 is diffuse during mitosis. Consequently, this pattern is considered as the reference and each initialization of any combination with pH3 ends with a diffuse pH3 pattern corresponding to the end of the cell cycle. This implies that the pH3 sequences are known and defined as $\mathbf{X}_i^{G-pH3}$ for each mouse $i$. A circular permutation is operated next to estimate the $X_i^{EdU-G}$ where $G \in \{E2F3A, E2F8, E2F4\}$ as follows:

$$\begin{aligned}
\min_{\left\{{}^{0-}\mathbf{X}_i^{EdU-G},\,{}^{0-}\mathbf{X}_i^{G-EdU}\right\}} \quad & \sum_{j=1}^{N_G}\left\|{}^{0-}\mathbf{X}_i^{G-EdU}-\mathbf{X}_j^{G-pH3}\right\|_2^2, \\
\text{subject to} \quad & {}^{0-}X_i^{G-EdU}(c) = {}^{\text{init}}X_i^{G-EdU}(c-q), q \in \{1,\dots,B\}, \\
& \forall i \in \{1,\dots,N_G\}, \forall G \in \{E2F3A, E2F8, E2F4\},
\end{aligned} \tag{19}$$

where $N_G = 3$ for $E2F3A$ and $E2F8$, $N_G = 2$ for $E2F4$, and ${}^{0-}X_i^{G-EdU}(c-q) = {}^{\text{init}}X_i^{G-EdU}(B-(c-q))$ if $(c-q)$ is negative. We solve this optimization problem by computing $\sum_{j=1}^{N_G}\|{}^{0-}\mathbf{X}_i^{G-EdU}-$

$\mathbf{X}_j^{G-pH3}\|_2^2$ for all possible shifts $c = \{1, \ldots, B\}$. The solution corresponds to the shift $c$ that gives the minimum sum. To better estimate EdU and initialize E2Fs, we now use the E2Fs expression:

$$\min_{\left\{{}^0\mathbf{X}_i^{EdU-G1}, {}^0\mathbf{X}_i^{G1-EdU}\right\}} \quad \sum_{j=1}^{N_{G1}} \left\| {}^0\mathbf{X}_i^{G1-EdU} - \mathbf{X}_j^{G1-pH3} \right\|_2^2 + \sum_{j=1}^{N_{G2}} \left\| {}^0\mathbf{X}_i^{EdU-G1} - {}^0\mathbf{X}_j^{EdU-G2} \right\|_2^2 + \sum_{j=1}^{N_{G3}} \left\| {}^0\mathbf{X}_i^{EdU-G1} - {}^0\mathbf{X}_j^{EdU-G3} \right\|_2^2, \tag{20}$$

$$\text{subject to} \quad {}^0X_i^{EdU-G1}(c) = {}^{0-}X_i^{EdU-G1}(c-q), q \in \{1, \ldots, B\}, \forall i \in \{1, \ldots, N_{G_1}\}$$

where $\{G1, G2, G3\}$ are successively $\{E2F3A, E2F8, E2F4\}$, $\{E2F8, E2F3A, E2F4\}$ and $\{E2F4, E2F8, E2F3A\}$, $N_{Gi} = 3$ if $Gi$ is $E2F3A$ or $E2F8$ and $N_{Gi} = 2$ if $Gi$ is $E2F4$. Again, we solve this optimization problem by computing the distances (20) for all possible shifts $c = \{1, \ldots, B\}$ and obtain the solution with the minimum value. Now, the temporal evolutions of EdU $\mathbf{X}_i^{EdU-G}$ and pH3 $\mathbf{X}_i^{pH3-G}$ are known for each mouse $i$ and each genotype $G \in \{E2F3A, E2F8, E2F4\}$. This implies that EdU and pH3 evolutions will not change but can be permuted for a given state of EdU or pH3. The E2Fs concentrations and patterns for EdU and pH3 after registration are shown in Fig. 4 supp. 4.

**Assignment problem** Now that EdU and pH3 are known, we define the estimation of E2Fs as an assignment problem where the goal is to find the permutations for each $\mathbf{X}_i^{G-M}, G \in \{E2F3A, E2F8, E2F4\}$ and $M \in \{EdU, pH3\}$ such that E2Fs accumulation over time are the most similar across data while EdU and pH3 are already known. We model this estimation as an assignment problem and

define the following square cost matrices:

$$
\begin{aligned}
Cost\left({}^{(z)}X_i^{G1-M1}(c_1,c_2)\right) = & \sum_{j=1}^{N_{G1}} \left\| {}^{(z-1)}X_i^{G1-M1}(c_1) - {}^{(z)}X_j^{G1-M2}(c_2) \right\|_2^2 + \\
& \sum_{j=1}^{N_{G2}} \left\| {}^{(z-1)}X_i^{G1-M1}(c_1) - {}^{(z)}X_j^{G1-G2}(c_2) \right\|_2^2 + \\
& \sum_{j=1}^{N_{G3}} \left\| {}^{(z-1)}X_i^{G1-M1}(c_1) - {}^{(z)}X_j^{G1-G3}(c_2) \right\|_2^2 + \\
& \left\| {}^{(z)}X_i^{M1-G1}(c_1) - X_i^{M1-G1}(c_2) \right\|_\infty + \\
& \frac{\sqrt{(c_1-c_2)^2}}{z}, \forall i \in \{1,\ldots,N_{G1}\},
\end{aligned} \tag{21}
$$

where the $\ell_\infty$ norm is used to ensure that EdU and pH3 states stay the same over the cell cycle, $\{G1, G2, G3\}$ are successively $\{E2F3A, E2F8, E2F4\}$, $\{E2F8, E2F3A, E2F4\}$ and $\{E2F4, E2F8, E2F3A\}$, $N_{Gi} = 3$ if $Gi$ is $E2F3A$ or $E2F8$ and $N_{Gi} = 2$ if $Gi$ is $E2F4$, $\{M1, M2\}$ are successively $\{EdU, pH3\}$ and $\{pH3, EdU\}$, $z$ corresponds to the iteration of the algorithm and:

$$
\begin{aligned}
Cost\left({}^{(z)}X_i^{E2F3A-G1}(c_1,c_2)\right) = & \sum_{j=1}^{3} \left\{ \left\| {}^{(z-1)}X_i^{E2F3A-G1}(c_1) - {}^{(z-1)}X_j^{E2F3A-EdU}(c_2) \right\|_2^2 + \right. \\
& \left. \left\| {}^{(z-1)}X_i^{E2F3A-G1}(c_1) - {}^{(z-1)}X_j^{E2F3A-pH3}(c_2) \right\|_2^2 \right\} + \\
& \sum_{j=1}^{N_{G1}} \left\{ \left\| {}^{(z-1)}X_i^{G1-E2F3A}(c_1) - {}^{(z-1)}X_j^{G1-EdU}(c_2) \right\|_2^2 + \right. \\
& \left. \left\| {}^{(z-1)}X_i^{G1-E2F3A}(c_1) - {}^{(z-1)}X_j^{G1-pH3}(c_2) \right\|_2^2 \right\} + \\
& \sum_{j=1}^{N_{G2}} \left\| {}^{(z-1)}X_i^{E2F3A-G1}(c_1) - {}^{(z-1)}X_j^{E2F3A-G2}(c_2) \right\|_2^2 + \\
& \frac{\sqrt{(c_1-c_2)^2}}{z}, \forall i \in \{1,\ldots,N_{G1}\},
\end{aligned} \tag{22}
$$

where $\{G1, G2\}$ are successively $\{E2F8, E2F4\}$ and $\{E2F4, E2F8\}$, $N_{Gi} = 3$ if $Gi$ is $E2F8$ and $N_{Gi} = 2$ if $Gi$ is $E2F4$. Each one of these five minimizations is processed one after another for iterations $z = \{1, \ldots, B\}$ by using the Hungarian algorithm (Kuhn 1955, Munkres 1957). In equation (21), the three first lines reflect the goal to have a given E2F accumulation over the cell cycle as similar as possible when combined with EdU, pH3 or another E2F; the fourth line corresponds to the constraint that EdU and pH3 are known and their state over the cell cycle cannot change, even though there can be permutations for a given state; and the last line defines a local constraint that forces permutations to be restricted in time for the first iterations and allows them to grow when iterations get larger. The latter constraint is used because the data is well initialized so the final estimation should not permute points directly all over the cell cycle. Equation (22) takes into account the differences between E2F3A accumulation over the cell cycle when combined with any marker or any other E2F, with the same constraint as in equation (21). Finally, a spline fitting is applied to each of the E2Fs across all experiments to get a final accumulation over the cell cycle, which is shown in Fig. 4. The code with the parameters used to estimate E2Fs accumulation over the cell cycle after initialization is available at `https://github.com/tpecot/EstimationOfProteinConcentrationOverTime`.

**Spatial distribution analysis**

The basement membrane and the lumen were manually annotated with the Annotater for each image. For each individual nucleus, the closest distance to the basement membrane and to the lumen were computed. These distances were pooled together for each genotype for each mouse

and QuantEv was used to generate Figs. 5 and 1 and to compute $p$-values.

## DATA AVAILABILITY

All the images used in this study are available at `https://data.mendeley.com/datasets/5r6kf37zd4/1`. The training datasets for nuclei segmentation are available at `https://github.com/tpecot/NucleiSegmentationAndMarkerIDentification/tree/master/UNet/datasets/nucleiSegmentation_E2Fs` for the U-Net architecture and at `https://github.com/tpecot/NucleiSegmentationAndMarkerIDentification/tree/master/MaskRCNN/datasets/nucleiSegmentation_E2Fs` for the Mask R-CNN architecture. The training datasets for nuclei segmentation and marker identification are available at `https://github.com/tpecot/NucleiSegmentationAndMarkerIDentification/tree/master/InceptionV3/trainingData` for the Inception-V3 architecture. The images used for the evaluation and the ground truth are available at the same locations than the training datasets. The intensity 2D histograms used to estimate the E2Fs accumulation over the cell cycle are available at `https://github.com/tpecot/EstimationOfProteinConcentrationOverTime/tree/master/data`.

## SOFTWARE AVAILABILITY

The codes used to train and process deep learning approaches for nuclei segmentations and marker identification are available at `https://github.com/tpecot/NucleiSegmentationAndMarkerIDentification`.

Archived code as time of publication: `https://doi.org/10.5281/zenodo.4619243`

Pécot (2021*c*)

License: GPL3

The Octave code used to estimate the E2Fs accumulation over the cell cycle is available at `https://github.com/tpecot/EstimationOfProteinConcentrationOverTime`.

Archived code as time of publication: `https://doi.org/10.5281/zenodo.4639800`

Pécot (2021*b*)

License: GPL3

The Java code of the Annotater plugin and the plugin are available at `https://github.com/tpecot/Annotater`. Video tutorials to show how to use the Annotater are available at the same location.

Archived code as time of publication: `https://doi.org/10.5281/zenodo.4639802`

Pécot (2021*a*)

License: GPL3

## REFERENCES

Abadi, M., Agarwal, A., Barham, P., Brevdo, E., Chen, Z., Citro, C., Corrado, G. S., Davis, A., Dean, J., Devin, M., Ghemawat, S., Goodfellow, I., Harp, A., Irving, G., Isard, M., Jia, Y., Jozefowicz, R., Kaiser, L., Kudlur, M., Levenberg, J., Mané, D., Monga, R., Moore, S.,

Murray, D., Olah, C., Schuster, M., Shlens, J., Steiner, B., Sutskever, I., Talwar, K., Tucker, P., Vanhoucke, V., Vasudevan, V., Viégas, F., Vinyals, O., Warden, P., Wattenberg, M., Wicke, M., Yu, Y. & Zheng, X. (2015), 'TensorFlow: Large-scale machine learning on heterogeneous systems'. Software available from tensorflow.org.

**URL:** *https://www.tensorflow.org/*

Blom, S., Paavolainen, L., Bychkov, D., Turkki, R., Mäki-Teeri, P., Hemmes, A., Välimäki, K., Lundin, J., Kallioniemi, O. & Pellinen, T. (2017), 'Systems pathology by multiplexed immunohistochemistry and whole-slide digital image analysis', *Scientific reports* **7**(1), 1–13.

Campton, D. E., Ramirez, A. B., Nordberg, J. J., Drovetto, N., Clein, A. C., Varshavskaya, P., Friemel, B. H., Quarre, S., Breman, A., Dorschner, M., Blau, S., Blau, C. A., Sabath, D. E., Stilwell, J. L. & Kaldjian, E. P. (2015), 'High-recovery visual identification and single-cell retrieval of circulating tumor cells for genomic analysis using a dual-technology platform integrated with automated immunofluorescence staining', *BMC cancer* **15**(1), 360.

Chen, H.-Z., Tsai, S.-Y. & Leone, G. (2009), 'Emerging roles of e2fs in cancer: an exit from cell cycle control', *Nature Reviews Cancer* **9**(11), 785–797.

Chollet, F. (2015), 'Keras'.

**URL:** *https://github.com/fchollet/keras*

Cireşan, D. C., Giusti, A., Gambardella, L. M. & Schmidhuber, J. (2013), Mitosis detection in breast cancer histology images with deep neural networks, *in* 'International conference on medical image computing and computer-assisted intervention', Springer, pp. 411–418.

Cireşan, D., Meier, U. & Schmidhuber, J. (2012), Multi-column deep neural networks for image classification, *in* '2012 IEEE conference on computer vision and pattern recognition', IEEE, pp. 3642–3649.

Cuitiño, M. C., Pécot, T., Sun, D., Kladney, R., Okano-Uchida, T., Shinde, N., Saeed, R., Perez-Castro, A. J., Webb, A., Liu, T., Bae, S. I., Clijsters, L., Selner, N., Coppola, V., Timmers, C., Ostrowski, M. C., Pagano, M. & Leone, G. (2019), 'Two distinct e2f transcriptional modules drive cell cycles and differentiation', *Cell reports* **27**(12), 3547–3560.

Falk, T., Mai, D., Bensch, R., Çiçek, Ö., Abdulkadir, A., Marrakchi, Y., Böhm, A., Deubner, J., Jäckel, Z., Seiwald, K., Dovzhenko, A., Tietz, O., Dal Bosco, C., Walsh, S., Saltukoglu, D., Tay, T. L., Prinz, M., Palme, K., Simons, M., Diester, I., Thomas, B. & Ronneberger, O. (2019), 'U-net: deep learning for cell counting, detection, and morphometry', *Nature methods* **16**(1), 67–70.

Grosse, A. S., Pressprich, M. F., Curley, L. B., Hamilton, K. L., Margolis, B., Hildebrand, J. D. & Gumucio, D. L. (2011), 'Cell dynamics in fetal intestinal epithelium: implications for intestinal growth and morphogenesis', *Development* **138**(20), 4423–4432.

He, K., Gkioxari, G., Dollár, P. & Girshick, R. (2017), Mask r-cnn, *in* 'Proceedings of the IEEE international conference on computer vision', pp. 2961–2969.

He, K., Zhang, X., Ren, S. & Sun, J. (2016), Deep residual learning for image recognition, *in* 'Proceedings of the IEEE conference on computer vision and pattern recognition', pp. 770–778.

Hollandi, R., Szkalisity, A., Toth, T., Tasnadi, E., Molnar, C., Mathe, B., Grexa, I., Molnar, J.,

Balind, A., Gorbe, M. et al. (2020), 'nucleaizer: a parameter-free deep learning framework for nucleus segmentation using image style transfer', *Cell Systems* **10**(5), 453–458.

Humbert, P. O., Rogers, C., Ganiatsas, S., Landsberg, R. L., Trimarchi, J. M., Dandapani, S., Brugnara, C., Erdman, S., Schrenzel, M., Bronson, R. T. & Lees, J. A. (2000), 'E2f4 is essential for normal erythrocyte maturation and neonatal viability', *Molecular cell* **6**(2), 281–291.

Iaquinta, P. J. & Lees, J. A. (2007), 'Life and death decisions by the e2f transcription factors', *Current opinion in cell biology* **19**(6), 649–657.

Jung, A. B., Wada, K., Crall, J., Tanaka, S., Graving, J., Reinders, C., Yadav, S., Banerjee, J., Vecsei, G., Kraft, A., Rui, Z., Borovec, J., Vallentin, C., Zhydenko, S., Pfeiffer, K., Cook, B., Fernández, I., De Rainville, F.-M., Weng, C.-H., Ayala-Acevedo, A., Meudec, R., Laporte, M. et al. (2020), 'imgaug'. Online; accessed 01-Feb-2020.

**URL:** *https://github.com/aleju/imgaug*

Keren, L., Bosse, M., Marquez, D., Angoshtari, R., Jain, S., Varma, S., Yang, S.-R., Kurian, A., Van Valen, D., West, R., Bendall, S. C. & Angelo, M. (2018), 'A structured tumor-immune microenvironment in triple negative breast cancer revealed by multiplexed ion beam imaging', *Cell* **174**(6), 1373–1387.

Krizhevsky, A., Sutskever, I. & Hinton, G. E. (2012), Imagenet classification with deep convolutional neural networks, *in* 'Advances in neural information processing systems', pp. 1097–1105.

Kuhn, H. W. (1955), 'The hungarian method for the assignment problem', *Naval research logistics quarterly* **2**(1-2), 83–97.

Lammens, T., Li, J., Leone, G. & De Veylder, L. (2009), 'Atypical e2fs: new players in the e2f transcription factor family', *Trends in cell biology* **19**(3), 111–118.

LeCun, Y., Bengio, Y. & Hinton, G. (2015), 'Deep learning', *nature* **521**(7553), 436–444.

Li, J., Ran, C., Li, E., Gordon, F., Comstock, G., Siddiqui, H., Cleghorn, W., Chen, H.-Z., Kornacker, K., Liu, C.-G., Pandit, S. K., Khanizadeh, M., Weinstein, M., Leone, G. & de Bruin, A. (2008), 'Synergistic function of e2f7 and e2f8 is essential for cell survival and embryonic development', *Developmental cell* **14**(1), 62–75.

Lin, T.-Y., Maire, M., Belongie, S., Hays, J., Perona, P., Ramanan, D., Dollár, P. & Zitnick, C. L. (2014), Microsoft coco: Common objects in context, *in* 'European conference on computer vision', Springer, pp. 740–755.

Lo, C.-A., Kays, I., Emran, F., Lin, T.-J., Cvetkovska, V. & Chen, B. E. (2015), 'Quantification of protein levels in single living cells', *Cell reports* **13**(11), 2634–2644.

Logan, N., Graham, A., Zhao, X., Fisher, R., Maiti, B., Leone, G. & La Thangue, N. B. (2005), 'E2f-8: an e2f family member with a similar organization of dna-binding domains to e2f-7', *Oncogene* **24**(31), 5000–5004.

Miyata, T. (2008), 'Development of three-dimensional architecture of the neuroepithelium: Role of pseudostratification and cellular 'community'', *Development, growth & differentiation* **50**, S105–S112.

Moen, E., Bannon, D., Kudo, T., Graf, W., Covert, M. & Van Valen, D. (2019), 'Deep learning for cellular image analysis', *Nature methods* pp. 1–14.

Munkres, J. (1957), 'Algorithms for the assignment and transportation problems', *Journal of the society for industrial and applied mathematics* **5**(1), 32–38.

Pécot, T. (2021*a*), 'Annotater'.

**URL:** *https://doi.org/10.5281/zenodo.4639802*

Pécot, T. (2021*b*), 'Estimation of protein concentration over time'.

**URL:** *https://doi.org/10.5281/zenodo.4639800*

Pécot, T. (2021*c*), 'Nuclei segmentation and marker identification'.

**URL:** *https://doi.org/10.5281/zenodo.4619243*

Pécot, T., Zengzhen, L., Boulanger, J., Salamero, J. & Kervrann, C. (2018), 'A quantitative approach for analyzing the spatio-temporal distribution of 3d intracellular events in fluorescence microscopy', *Elife* **7**, e32311.

Pitarresi, J. R., Liu, X., Sharma, S. M., Cuitiño, M. C., Kladney, R. D., Mace, T. A., Donohue, S., Nayak, S. G., Qu, C., Lee, J., Woelke, S. A., Trela, S., LaPak, K., Yu, L., McElroy, J., Rosol, T. J., Shakya, R., Ludwig, T., Lesinski, G. B., Fernandez, S. A., Konieczny, S. F., Leone, G., Wu, J. & Ostrowski, M. C. (2016), 'Stromal ets2 regulates chemokine production and immune cell recruitment during acinar-to-ductal metaplasia', *Neoplasia* **18**(9), 541–552.

Rempel, R. E., Saenz-Robles, M. T., Storms, R., Morham, S., Ishida, S., Engel, A., Jakoi, L., Melhem, M. F., Pipas, J. M., Smith, C. & Nevins, J. R. (2000), 'Loss of e2f4 activity leads to abnormal development of multiple cellular lineages', *Molecular cell* **6**(2), 293–306.

Ronneberger, O., Fischer, P. & Brox, T. (2015), U-net: Convolutional networks for biomedical image segmentation, *in* 'International Conference on Medical image computing and computer-assisted intervention', Springer, pp. 234–241.

Schindelin, J., Arganda-Carreras, I., Frise, E., Kaynig, V., Longair, M., Pietzsch, T., Preibisch, S., Rueden, C., Saalfeld, S., Schmid, B., Tinevez, J.-Y., James White, D., Hartenstein, V., Eliceiri, K., Tomancak, P. & Cardona, A. (2012), 'Fiji: an open-source platform for biological-image analysis', *Nature methods* **9**(7), 676–682.

Schmidhuber, J. (2015), 'Deep learning in neural networks: An overview', *Neural networks* **61**, 85–117.

Schneider, C. A., Rasband, W. S. & Eliceiri, K. W. (2012), 'Nih image to imagej: 25 years of image analysis', *Nature methods* **9**(7), 671–675.

Szegedy, C., Vanhoucke, V., Ioffe, S., Shlens, J. & Wojna, Z. (2016), Rethinking the inception architecture for computer vision, *in* 'Proceedings of the IEEE conference on computer vision and pattern recognition', pp. 2818–2826.

Tsai, S.-Y., Opavsky, R., Sharma, N., Wu, L., Naidu, S., Nolan, E., Feria-Arias, E., Timmers, C., Opavska, J., De Bruin, A., Chong, J.-L., Trikha, P., Fernandez, S. A., Stromberg, P., Rosol, T. J. & Gustavo, L. (2008), 'Mouse development with a single e2f activator', *Nature* **454**(7208), 1137–1141.

Ueno, M., Katayama, K.-i., Yamauchi, H., Nakayama, H. & Doi, K. (2006), 'Cell cycle progression is required for nuclear migration of neural progenitor cells', *Brain research* **1088**(1), 57–67.

Van der Walt, S., Colbert, S. C. & Varoquaux, G. (2011), 'The numpy array: a structure for efficient numerical computation', *Computing in Science & Engineering* **13**(2), 22–30.

Van der Walt, S., Schönberger, J. L., Nunez-Iglesias, J., Boulogne, F., Warner, J. D., Yager, N., Gouillart, E. & Yu, T. (2014), 'scikit-image: image processing in python', *PeerJ* **2**, e453.

Van Valen, D. A., Kudo, T., Lane, K. M., Macklin, D. N., Quach, N. T., DeFelice, M. M., Maayan, I., Tanouchi, Y., Ashley, E. A. & Covert, M. W. (2016), 'Deep learning automates the quantitative analysis of individual cells in live-cell imaging experiments', *PLoS computational biology* **12**(11).

Vincent, L. & Soille, P. (1991), 'Watersheds in digital spaces: an efficient algorithm based on immersion simulations', *IEEE Transactions on Pattern Analysis & Machine Intelligence* (6), 583–598.

Virtanen, P., Gommers, R., Oliphant, T. E., Haberland, M., Reddy, T., Cournapeau, D., Burovski, E., Peterson, P., Weckesser, W., Bright, J., van der Walt, S. J., Brett, M., Wilson, J., Jarrod Millman, K., Mayorov, N., Nelson, A. R. J., Jones, E., Kern, R., Larson, E., Carey, C., Polat, İ., Feng, Y., Moore, E. W., Vand erPlas, J., Laxalde, D., Perktold, J., Cimrman, R., Henriksen, I., Quintero, E. A., Harris, C. R., Archibald, A. M., Ribeiro, A. H., Pedregosa, F., van Mulbregt, P. & Contributors, S. . . (2020), 'SciPy 1.0: Fundamental Algorithms for Scientific Computing in Python', *Nature Methods* .